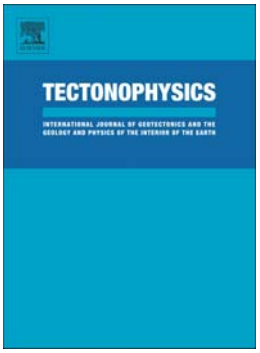

Thickness of the oceanic crust, the lithosphere, and the mantle transition zone in the vicinity of the Tristan da Cunha hot spot estimated from ocean-bottom and ocean-island seismometer receiver functions

Wolfram H. Geissler, Wilfried Jokat, Marion Jegen, Kiyoshi Baba

PII: S0040-1951(16)30612-6
DOI: doi: 10.1016/j.tecto.2016.12.013
Reference: TECTO 127356

To appear in: *Tectonophysics*

Received date: 29 February 2016
Revised date: 28 November 2016
Accepted date: 9 December 2016

Please cite this article as: Geissler, Wolfram H., Jokat, Wilfried, Jegen, Marion, Baba, Kiyoshi, Thickness of the oceanic crust, the lithosphere, and the mantle transition zone in the vicinity of the Tristan da Cunha hot spot estimated from ocean-bottom and ocean-island seismometer receiver functions, *Tectonophysics* (2016), doi: 10.1016/j.tecto.2016.12.013

Thickness of the oceanic crust, the lithosphere, and the mantle transition zone in the vicinity of the Tristan da Cunha hot spot estimated from ocean-bottom and ocean-island seismometer receiver functions

Wolfram H. Geissler[1], Wilfried Jokat[1,4], Marion Jegen[2], Kiyoshi Baba[3]

[1]Alfred Wegener Institute, Helmholtz Centre for Polar Research, Am Alten Hafen 26, 27568 Bremerhaven, Germany

[2]GEOMAR, Helmholtz Centre of Ocean Research Kiel, Wischhofstr. 1-3, 24148 Kiel, Germany

[3]Earthquake Research Institute, The University of Tokyo, 1-1-1 Yayoi, Bunkyo-ku, Tokyo 113-0032, Japan

[4]University of Bremen, Geoscience department, Bremen, Germany

Abstract

The most prominent hotspot in the South Atlantic is Tristan da Cunha, which is widely considered to be underlain by a mantle plume. But the existence, location and size of this mantle plume have not been established due to the lack of regional geophysical observations. A passive seismic experiment using ocean bottom seismometers aims to investigate the lithosphere and upper mantle structure beneath the hotspot. Using the Ps receiver function method we calculate a thickness of 5 to 8 km for the oceanic crust at 17 ocean-bottom stations deployed around the islands. Within the errors of the method the thickness of the oceanic crust is very close to the global mean. The Tristan hotspot seems to have contributed little additional magmatic material or heat to the melting zone at the mid-oceanic ridge, which could be detected as thickened oceanic crust. Magmatic activity on the archipelago and surrounding seamounts seems to have only effected the crustal thickness locally. Furthermore, we imaged the mantle transition zone discontinuities by analysing receiver functions at the permanent seismological station TRIS and surrounding OBS stations. Our

observations provide evidence for a thickened (cold) mantle transition zone west and northwest of the islands, which excludes the presence of a deep-reaching mantle plume. We have some indications of a thinned, hot mantle transition zone south of Tristan da Cunha inferred from sparse and noisy observations, which might indicate the location of a Tristan mantle plume at mid-mantle depths. Sp receiver functions image the base of lithosphere at about 60 to 75 km beneath the islands, which argues for a compositionally controlled seismological lithosphere-asthenosphere boundary beneath the study area.

Keywords:

Receiver functions

Ocean-bottom seismometer

Oceanic crust

Mantle transition zone

Hot spot

Tristan da Cunha

1. Introduction

According to classic plume theory (Morgan, 1971), the Tristan da Cunha mantle plume played a major role in the rifting of the South Atlantic margins by impinging at the base of the continental lithosphere shortly before or during the breakup of the South Atlantic. Onshore the Tristan mantle plume is associated with the emplacement of the Parana-Etendeka flood basalt province ~132 Ma, and offshore with the age-progressive Walvis Ridge and associated young seamount province (Gibson et al., 2006; O'Connor and Duncan, 1990; O'Connor et al., 2012; Rohde et al., 2013).

Following Courtillot et al. (2003) and French and Romanovicz (2015), the mantle plume beneath the Tristan da Cunha hot spot is "primary" or "clearly resolved". French and Romanovicz (2015) show that it is connected to a large low-velocity structure in the lower mantle and an ultra-low velocity zone at the core-mantle boundary. However, the global data (French and Romanovicz, 2015) is lacking coverage and therefore resolution around the Tristan da Cunha for shallower mantle depths. Thus, the existence of a deep Tristan da Cunha mantle plume is still controversial. The hotspot at Tristan da Cunha might instead be caused by convective processes in the shallow mantle (plate model, see Anderson, 2005) that may actually be a consequence of the South Atlantic opening. The equivocal character of Tristan da Cunha is largely due to a lack of regional geophysical and petrological data.

The search for a deep-reaching geophysical/thermal anomalies beneath Tristan da Cunha was the starting point for a multi-disciplinary geophysical experiment to acquire passive marine electromagnetic and seismic data, and bathymetric data within the framework of the SPP1375 **S**outh **A**tlantic **M**argin **P**rocesses and **L**inks with onshore **E**volution (SAMPLE) funded by the German Science foundation. The experiment included two expeditions with the German research vessel MARIA S. MERIAN in 2012 and 2013.

In order to study the imprint of a mantle plume by means of converted teleseismic phases (receiver functions) we concentrate here on the thickness of the magmatic oceanic crust. If a mantle plume interacts with a nearby mid-ocean ridge, the increased heat and melt budget should result in a thickening of the oceanic crust, acc. to White et al. (1992). Local estimates of lithosphere thickness might also help to understand if the seismologically defined lithosphere-asthenosphere boundary is controlled by thermal structure and plate cooling (e.g., Parson and Sclater, 1977) or

by changes in composition due to melt depletion and dehydration (e.g., Gaherty et al., 1996). Furthermore, we will try to detect anomalies within and at the base of the lithosphere, and in the upper mantle that might be caused by thermal and magmatic rejuvenation. Finally, we try to identify plume-related thermal anomalies in the mantle transition zone that should distort the mineral phase transitions at about 410 and 660 km depth (Helffrich, 2000; Li et al., 2003), which would provide evidence for a lower-mantle origin for the mantle plume.

2. Data and method

Experiment

Between February 2012 and January 2013, a network of 24 ocean-bottom seismometers (OBS) from the German DEPAS pool (Deutscher Geräte-Pool für Amphibische Seismologie) and 26 ocean-bottom magneto-telluric stations from GEOMAR Kiel and the University of Tokyo were deployed around the archipelago of Tristan da Cunha (Geissler, 2014) (Fig. 1). The seismological stations are equipped with a Güralp CMG-40T broadband seismometer (60 s) incorporated in a titanium pressure housing, a hydrophone, and a GEOLON MCS (**M**arine **C**ompact **S**eismocorder) data logger from SEND GmbH Hamburg, Germany. Each sensor channel is sampled at 50 Hz (2 BBOBS at 100 Hz), preamplifier gain of the hydrophone channel is 4 and 1 for the three seismometer components. The seismometers are connected to a cardanic levelling mechanism, which was activated every 21 days to level the sensors.

To complement the ocean-bottom network and the existing observatory on Tristan da Cunha (TRIS), two land seismometers and one magnetotelluric station were installed on Nightingale Island located southwest of the main island each of which

was equipped with a Güralp-3ESP seismometer (60 s) and an EarthData data logger. As recording parameters we chose 100 Hz sampling rate and low preamplifier gain (0.4). One of the stations (Fig. 1; NIG01) recorded earthquake data for the entire year, while the second station failed after few days due to water damage. Unfortunately, the permanent station TRIS failed also during the experiment. We used instead for our study seismological data recorded by TRIS in the period 07/2004 till 01/2012.

OBS and ocean island seismological data are known to be very noisy. Therefore, we could only analyse very few (2-10) events that had a sufficient signal to noise ratio. We had to also apply a narrow band pass filter. For the permanent station TRIS, we applied a high pass of 50 s in combination with multiple low pass filters between 1 s and 10 s. For most of the OBS stations, we used 12 s or 20 s as the high pass. Best results for calculating the crustal thickness could be achieved with a low pass of 2 s or 3 s, whereas, we had to apply a low pass of 7 s to study the mantle transition zone discontinuities at the TRIS and the OBS stations..

Method

The Ps receiver function method (e.g., Vinnik, 1977, Kind et al., 1995 and Yuan et al., 1997) is a common approach to study lithospheric and upper-mantle seismic discontinuities beneath continents. There have been also a few studies analysing receiver functions from ocean-bottom data (e.g., Kumar and Kawakatsu, 2011; Kumar et al., 2011; Suetsugu et al., 2005, 2009; Leahy et al., 2010). To separate the primary and converted phases, we perform the rotation from the Z, N–S and E–W (ZNE) components into the P, SV and SH system (LQT components). Since the distribution of good seismic events in the distance range of 30 to 97 degrees was very limited

during our deployment, we also used PP as primary phases. PP phases have been used used previously, e.g., by Yuan et al. (2006a).

A major problem regarding OBS data is that the exact orientation of the horizontal components X and Y is not known and has to be determined from the data itself. We estimated the back azimuth from polarization analysis of the horizontal components. The angles of incidence were determined by minimizing the energy on the SV component (Q) at the time of the P signal (Kind et al. 1995). Since the OBSs were deployed in the central part of the South Atlantic, there are few or only very thin sediments so the waveform should not be disturbed by a shallow low-velocity layer beneath the stations. We did not correct for any water layer effects during the processing because the velocity contrast between the oceanic crust and the water layer is high. However, the water layer was included in the calculation of synthetic receiver functions (see below).

To remove the source signal and any source-side reverberations, we used a time-domain deconvolution method (Kind et al., 1995). Amplitudes of the SV and SH components were normalized in relation to the incident P wave. Arrival times were measured at the maximum of the deconvolved P-wave signal. iasp91 velocity model (Kennett 1991) was used for the moveout correction to the fixed reference epicentral distance of 67º (slowness: 6.4 s deg^{-1}).

We estimated the crustal thickness and average Vp/Vs ratio by applying the method introduced by Zhu and Kanamori (2000). In order to study the effect of the water layer and a thin oceanic crust, we analysed synthetic seismograms in the same way as for real data. The reflectivity method was used to compute the theoretical seismograms (Fuchs and Müller, 1971; Wang, 1999).

To study the depth to base of lithosphere, we applied the Sp receiver function method (e.g., Bock, 1991) to data recorded at station TRIS (see Yuan et al., 2006b; Geissler et al., 2012 for details). Sp and SKSp converted phases from the lithosphere-asthenosphere boundary are not masked by crustal multiples, since these phases arrive before the primary S and SKS phases. We analysed the data without restitution of true ground displacement to retain the higher frequencies in the recordings. Further processing steps are move-out corrections for slowness of 6.4 s/° as previously applied during Ps receiver function processing.

3. Results

Crustal Structure

Figure 2 shows the stacks of moveout-corrected receiver functions for two island stations, the sum of all OBS traces (TDCXX), and the single OBS TDC26 for different period ranges. Stacks for the remaining stations and stacks of subsets of OBS stations are shown in Appendix 1. In all cases, there are clear phases with different polarities visible in the first 6 seconds delay time. It is obvious from stations TRIS and TDC26 and the stacks of TDCXX that the first two positive polarity phases (blue dashed lines in Fig. 2), which can be seen at high frequencies, merge into one positive polarity phase at lower frequencies. These phases are followed by a strong consistent negative polarity phase at delay times of 3 to 6 seconds (red dashed line in Fig. 2). Assuming that most of the stations are located on normal oceanic crust, we assume that all these phases are related to crustal structure. There is only a thin sedimentary cover in the area, and in some areas basalt is outcropping on the seafloor. We observe additional phases at later delay times (>6 s) at most of the OBS stations and also at NIG01. These might be strongly influenced by noise conditions and most

probably water layer reverberations (e.g., the phases marked by yellow dashed lines in Fig. 2). Therefore, we did not try to interpret these phases. The influence of the water layer increases at lower periods (see synthetic receiver functions below).

As already described above, we see a clear negative phase at about 3 to 4 s at the OBS stations and at about 6 s at station TRIS (see Figure 2, Table 1, Appendix 1). This phase might be a multiple from the Moho. Inverting the data from TRIS for crustal thickness and Vp/Vs ratio (Zhu and Kanamori 2000) gives 9.4 km and 1.78, respectively (average crustal seismic velocity Vp = 6 km/s), see Figure 3. Stacking all traces observed at OBS stations together, we get 5.8 km and 1.87, respectively (Fig. 3. Table 1). Whereas the Vp/Vs ratio is not well determined, the crustal thickness should be resolved within an uncertainty of 1 to 2 km.

Figure 4 shows stacked receiver functions for all analysed stations in the period ranges of 2 s and 3 s to 20 s, respectively. Further period ranges are plotted in Appendix 2. The most consistent phase is the negative phase at about 3 to 6 s (Fig. 4, red dashed lines). It is followed by quite consistent, positive polarity phases (yellow dashed lines), but they are difficult to interpret. We attribute these phases mainly to reverberations in the water layer (see also below). At the two island stations (TRIS and NIG01), as well as at the nearby OBS station TDC26, we identify the primary or mixed primary/first multiple converted phases from the crust mantle boundary (blue dashed lines). There are additional negative phases observed below stations TRIS and NIG01 that are difficult to understand at first glance that we discuss below.

Mantle transition zone

To study the discontinuities of the mantle transition zone at ~410 (“410”) and ~660 (“660”) km depth, high-quality observations are needed to identify potential thermal

effects at the associated phase transitions. Therefore, we decided to analyse the data from the permanent observatory TRIS separately because of the larger data set available. But, not surprisingly, most of the good observations at TRIS are from events located to the west and northwest along the South and Central American subduction zones. We had to rely on PP as primary phases to study also the eastern and southern sectors of the study area. Figure 5 shows sum traces for different period ranges (Fig. 5a) and three different backazimuth sectors (Fig. 5c), whereas Appendix 3 show sum traces for primary P and PP phases separately. Delay times are compiled in Table 2.

Within the NE backazimuth sector (0°-140°), 14 mainly PP phases were used for this study. No coherent primary converted phase from the "410" can be observed (Fig. 5c, Appendix 4). Due to the minimal difference in epicentral distances we cannot clearly distinguish between primary and multiple converted phases by correcting for the corresponding moveout. The P660s arrives at 67.7 s delay time (amplitude 0.08 relative to primary P amplitude), slightly before the theoretical delay time of 68.1 s of the iasp91 Earth velocity model. Since only one phase can be clearly detected, we cannot estimate the thickness (differential delay time) of the mantle transition zone.

Within the S backazimuth sector (140°-210°), 16 PP phases had to be used for the analyses (Fig. 5c, Appendix 4). The sum trace for primary converted phases (S PS in Fig. 5c) looks noisy with many phases between the crustal phases and the mantle transition zone, which makes any interpretation more difficult. Also, the stacking for different move-out (for primary and multiple converted phases) does not help to identify primary phases with higher confidence. A potential P410s can be observed at 45.3 s delay time (relative amplitude 0.16). That would be more than a second later than the theoretical arrival time of 44.1 s. Two phases can be observed close to the

theoretical delay time of the "660", the first one at 65.6 s (relative amplitude 0.08), the second at 72.1 s (relative amplitude 0.12). Therefore, the thickness (differential delay time) of the mantle transition zone might be 20.3 s or 26.8 s, which, if our phase identifications are correct, is thinner or thicker than derived from the iasp91 velocity model (24 s),

The best observation of the mantle transition zone discontinuities can be made NW of station TRIS (backazimuth range 210°-360°), since most of the primary P phases arrive from South/Central America (Fig. 5c, Appendix 4). Stacking only the 13 highest quality traces, we can clearly detect the P410s and P660s at 43.7 s (relative amplitude 0.05) and 69.0 s (relative amplitude 0.07), respectively. This indicates that the mantle transition zone is thickened to 25.3 s differential delay time and therefore more than 1 s thicker than the global model. In contrast to the other two sectors, the stacking for different moveout clearly helps to identify both interpreted phases as primary converted phases from the mantle transition zone.

The temporary OBS and land stations observe the converted phases from the mantle transition zone with higher uncertainty, since the data are more sparse and noisy (Fig. 5b and d, Appendix 5). As can be seen from figure 5b, the longer period observations of the P410s might be affected by the water layer reverberations. The observations of the P660s seem to be more consistent, at least in the stacks of all OBS traces (Fig. 5b). Since we want to study the mantle at 410 and 660 depth we grouped and stacked the individual receiver functions according to their piercing points in 410 km depth (see below in figure 10) applying a kind of common piercing point stacking approach. We could make phase identifications that follow the trend of the observations made at station TRIS. At the westernmost stack TDC-A just below the Mid-Atlantic Ridge to the west of Tristan da Cunha (Fig. 5d) we see a potential 410

km conversion at 41.9 s and a 660 km conversion at 69.7 s delay time. Whereas the first phase is not reliable, the second deeper phase stands out more clear. Unfortunately, the data does not allow unambiguous phase identifications based on the moveout of phases.

TDC-B stacks traces with piercing points SW of Tristan da Cunha. Again, the P410s is not as clear as the P660s. Both phases arrive slightly earlier than predicted by the iasp91 velocity model (see Table 2) and the differential delay time of 24.8 s predict a slightly thickened mantle transition zone comparable to TRIS-NW.

The P410s of stack TDC-C is more pronounced than the P660s (Fig. 5d). If the phase identification of the P410s is correct, the delay time of 48.6 s implies very low seismic shear wave velocities in the upper mantle, since there is a time difference of 4.5 s to the theoretical delay time of 44.1 s. The differential delay time of 19.3 s indicates an even thinner mantle transition zone than observed at TRIS-S. But again, as stated above, unambiguous phase identification is not possible.

Stack TDC-D only includes five traces (Fig. 5d). That might be too few since no clear coherent phases are observed at delay times predicted by the iasp91 velocity model.

As shown by Geissler et al. (2008), the uncertainty of P410s and P660s measured at temporary land stations might be in the order of 0.5 s to 1.0 s. Since we can only analyse very few events at the permanent observatory TRIS as is normal for temporary deployments, we might adopt this error estimate. The uncertainty for the observations at the OBS stations is most probably 1.0 s or slightly larger. The amount of available data does not allow for a better error estimate.

Synthetic receiver functions

In order to better understand the noisy phases, we computed receiver functions from synthetic seismograms (Fig. 7) using the reflectivity method (Kind 1985; Wang, 1999). We used a simple model to understand the response of a 7 km thick single layer oceanic crust above the upper mantle in different period ranges (model M4) and the effect of an additional water layer (model M3), see appendix 6 for the model. The receiver was placed 1 m beneath the surface (model M4) or seafloor (model M3), respectively. Looking at the receiver functions calculated for model M4 we can see clearly that the primary and the first multiple conversions are separate phases at high frequencies, but merge at lower frequencies. But the second negative polarity multiple (PpSs+PsPs) stands out clearly and it's delay time does not change significantly. This shows that this phase is a very good candidate for studying crustal thickness, much better than the primary and first multiple conversions. As can be seen from model M3, the water layer seems have had only a minor effect at high frequencies. But from a low pass of at least 5 s, the final receiver functions are distorted by water layer effects/reverberations and do not allow for a detailed crustal study. In both models the converted phases from the mantle transition zone stand out clearly. It should be taken into account that natural noise would make proper phase identifications more difficult.

Forward modelling

To verify our phase identifications, we also applied the forward modelling approach (Kind et al. 1995; Geissler et al. 2012). We tried to fit the first phases with a simple ocean crust model. The velocity structure within the crust is constrained by results from wide-angle seismic studies across the Walvis Ridge and the Discovery Seamount (Jokat and Kessling, 2017). A constant Vp/Vs ratio of 1.80 was used for the

crust and the upper mantle to model the crustal structure. Density was adjusted following Birch's law (Birch, 1961). Figure 7 shows the results for stations TDC26, NIG01, and TRIS. Models are tabulated in Appendix 7.

OBS station TDC26 (model tdc26_2.1b, Fig. 7a) can be modelled as 5.5 km thick two-layered oceanic crust on top of a normal upper mantle, disregarding later spurious arrivals. To constrain the crustal thickness, the negative polarity phase at about 4 s is the most important. The earlier positive polarity phases are also influenced by the internal crustal structure and might therefore be misleading when calculating crustal thicknesses. A similar effect can be seen at station NIG01 (fig. 7c). Here, the best fit to the first observed phases within 6 s delay time can be achieved by a two-layer oceanic crust with a thickness of only 6 km (model nig01_2.1b). This seems to be very thin considering that the island rises 3 km above the surrounding seafloor. By deepening the Moho to 18 km depth (model nig01_2.1c), we are able to fit the minimum at 10 s delay time. A reasonable fit to the waveform within the first 12 s delay time can be achieved with a more complex crust-mantle transition between 6 and 18 km depth (model nig01_2.1d).

A very good fit can be achieved for station TRIS within 10 s delay time (model tris_2.1b, Fig. 7b). This is not a surprise since there are much more data available and the noise can be suppressed by careful event selection and stacking. The simplest model shows an oceanic-like crust, slightly thickened to 9 km. Considering that the island rises >3.5 km above to the surrounding seafloor (relative elevation of the station), the thickness of the underlying crust is about 5.5 km. However, the thickness beneath the central part of the island might be larger, since most of our observations stem from an area NW of the island, that means from below the island NW flank and normal adjacent seafloor.

Looking at Figs 2 and 7, an additional negative polarity phase can be observed at TRIS at about 16 s delay time flanked by two positive polarity phases. This is true for the period ranges up to 5 s low pass. For 7 s low pass, a similar phase is observed, but at later delay times (see Figs 2 and 5a), which is a bit curious. However, we tried to find a model that explain these phases at 16 s. Li et al. (2000) observed similar phases at station HIBSN on Hawaii and modelled them as the response of a low velocity layer in about 130 to 170 km depth. In model tris_2.3b (Fig. 7d) we can explain these phases with a low-velocity/high Vp/Vs layer in a depth of about 140 to 150 km. Model tris_2.3b includes a lithosphere-asthenosphere transition at 50 to 65 km depth. But such a velocity transition zone does not have a large and therefore visible effect in the waveform. By accident, the arrival of the LAB phase falls together with the second negative polarity multiple of the crust. That's why the modelled amplitude is larger at about 5 s delay time for model tris_2.3b in comparison to model tris_2.1b.

Woelbern et al. (2006) modelled a negative phase at 24 s delay time observed at station KIP on Hawaii as the multiple of a sharp lithosphere-asthenosphere boundary at 65 km depth. Modelling our negative phase at 16 s (station TRIS) as the multiple of a sharp LAB would results in a LAB depth of about 45-46 km, but in this case the primary conversion arriving at a similar time as the Moho multiple should be much stronger than observed in our data (see Fig. 8). Therefore, we do not assume the existence of a very sharp lithosphere-asthenosphere boundary at 45 km depth beneath TRIS.

Sp Receiver Functions

Figure 8a shows stacks of all Sp and SKSp receiver functions observed at station TRIS for two different frequency bands. Depending on the low pass chosen, we

observe two (low pass 7 s) or one (low pass 10 s) positive polarity phases up to 6 s lead time. The first of the two phases observed at 7 s low pass stems most probably from the Moho beneath the island in accordance with the results from Ps receiver functions. The second positive phase at 5.2 s is more difficult to explain. Since S receiver functions are not masked by crustal multiples, these phases should originate at an intra-lithospheric discontinuity beneath the islands. At about 8 second lead time we observe a very coherent negative polarity phase, which we attribute to the base of the lithosphere. Since the piercing points of Sp and SKSp phases in 60 km depth are located about 15 and 70 km away from the station, respectively, the stacks give some average smoothed lithospheric thickness estimate. The results obtained for a low pass of 7 s do not differ dramatically from the results obtained with a low pass of 10 s, see Tab. 3. However, for the SKSp stack at 10-s low pass we observe the maximum of the negative phase at 6.6 s lead time.

We tried also to study variations in lithospheric thickness around station TRIS by separating the Sp and SKSp receiver functions according to their primary phases and backzimuth distribution. The stacks are shown in Fig. 8b (for single traces see Appendix 8). We only show these results since the observations are more coherent at 10-second low pass. Results obtained for a low pass of 7 seconds are listed in Tab. 3. As can be seen from Figure 10 and Table 3, we observe prominent negative polarity phases at almost all backazimuth ranges, with the exception of the one to the south (140°-240°). The most reliable observations stem from the eastern and western sectors. The lead times range from 6.8 to 8.1 s. As already discussed there are also positive polarity phases between 2 and 5 s lead time, which might stem from intra-lithospheric discontinuities beneath the islands.

4. Interpretation

Crustal thickness

As explained and shown above, the negative polarity phase between 3 and 6 s delay time (Fig. 4; red dashed line) can be interpreted as the PpSs+PsPs multiple of the Moho and does not have to originate at the top of a low velocity zone (lithosphere-asthenosphere boundary), which is the common interpretation in receiver function literature for ocean island stations (e.g., Haldar et al., 2005). The origin of this high-amplitude phase as a multiple is the most simple and profound interpretation, since no complicated velocity structure is needed. Therefore, the delay time of this negative polarity phase can be taken as a proxy of the thickness of oceanic crust. It is even better suited than the earlier primary converted phases due to the interference of the primary and first multiple phases. Following Zandt et al. (1995), the delay time of PpSs+PsPs multiple can be calculated through

(1) $t_{PpSs+PsPs} = 2\ H\ (\ 1 / Vs^2 - p^2)^{1/2}$.

Transforming equation (1) and taking a reference slowness p of 6.4 s/° (corresponding to an epicentral distance of 67°), an average crustal Vp velocity of 6 km/s and a Vp/Vs ratio of 1.80 (meaning Vs of 3.33 km/s), we end up with the relation

(2) H (crustal thickness / km) = $t_{PpSs+PsPs}$ (PpSs+PsPs delay time / s) / 0.59

This approach allows us to map the thickness of the oceanic crust in the vicinity of Tristan da Cunha, even using noisy OBS data. The uncertainty of the PpSs+PsPs delay time observations estimated from the differences observed between the

measurements in different period ranges is about 0.3 s for good stations, but could be as large as 1.2 s for more noisy stations (see Table 1). This translates into an uncertainty of the estimated crustal thickness on the order of between ±0.5 km and ±2 km. There might be a bias of 0.5 km due to the used average crustal Vp velocity and Vp/Vs ratio.

As can be seen in Figure 9, the crustal thicknesses range from 5.5 to 8.5 km. According to global age grids, the oceanic lithosphere beneath the study area is between 10 Ma and 30 Ma old (Mueller et al., 2008, Fig. 9). The crustal thickness estimates, within the uncertainties discussed above, are very close to the mean crustal thickness of normal oceanic crust of 7 km (White et al., 1992), which is surprising close to a primary hotspot like Tristan da Cunha. Even below the currently active Tristan da Cunha Island, the crust seems to not be significantly thickened. Station TDC12 indicate a crustal thickness of 8.5 km, whereas beneath Tristan da Cunha itself and Nightingale Island the original oceanic crust beneath the later built-on islands seems to be only 7 and 6 km thick, respectively. However, waveforms at stations TDC12, TDC14 (see Appendix 1) and NIG01 (Fig. 7, see also Weit et al., in press) imply that the shallow lithosphere in vicinity to the volcanic edifices is somehow modified, most probably by magmatic intrusions. The general normal oceanic crustal thickness also concurs with the results of Jokat and Kessling (2017) along the older part of the Walvis Ridge, which only show thickened crust immediately beneath its seamounts. The consequence of this finding might be that no large-scale contribution of plume mantle or heat from Tristan hotspot toward the mid-ocean ridge melting zone exists in our research area for the last 30 Ma. Otherwise increased crustal production at the mid-oceanic ridge would have significantly increased crustal thickness. There seems to be a minor tendency for thinner crust

(about 0.5 to 1 km) beneath the southwestern stations compared to stations further to the north and east.

Mantle transition zone

The mantle transition zone seems to be thickened by about one second (~10 km) between the Tristan da Cunha archipelago and the Mid-Atlantic ridge (Figs 5 and 10; Tab. 2). Additionally, the P410s arrive slightly earlier than predicted by the iasp91 velocity model, implying higher average velocities/lower average Vp/Vs ratio in the upper mantle (Geissler et al., 2008). This is quite unusual in close vicinity to a hotspot. Early arrivals of the P410s and thickened mantle transition zones were not reported by Li et al. (2003) for a suite of other globally spread hot spots. For the sector northeast of Tristan da Cunha we do not have an observation of a P410s, but here the P660s seem to arrive again earlier than predicted by the reference model (TRIS-NE), implying higher average velocities/lower average Vp/Vs ratio in the upper mantle, which is not consistent with a mantle plume penetrating the mantle transition zone in this area. But we cannot rule out a real shallowing of the "660" in the area. A hot mantle plume should leave a positive thermal imprint on the phase transitions at 410 and 660 km depth, in case of an olivine-dominated lithology (Helffrich, 2000; Lebedev et al., 2002). There are two explanations for our observations. Either the mantle composition to the west, north and east is not influenced by any hot uprising material and the transition zone is rather cold, or the lithology at mid-mantle depths is not purely dominated by olivine, but also by aluminium (garnet)-rich phases (see Simmons and Gurrola, 2000). The generally high velocities observed in global models for the mantle transition zone beneath the South

Atlantic (Gu and Dziewonski, 2002; Lebedev and van der Hilst, 2008) would support the first explanation.

The only area that concurs with the presence of a hot mantle plume disturbing the phase transitions at mid-mantle depths might be the area directly beneath the islands (slightly shifted westward), and to the south of the Tristan da Cunha Fracture Zone (Fig. 10), an area with elevated seafloor topography. Unfortunately, here our data are sparse and noisier, since only PP phases could be used for the analysis at station TRIS. P410s observed at TRIS-S exhibits a delay of more than one second in comparison to the reference model. Li et al. (2003) observed similarly delayed P410s phases at stations WAKE (Wake Island) and XMAS (Kiritimati Island) located at hotspots in the Pacific. The delay, if it is true, could be best explained as the effect of low velocities in the upper mantle (Li et al., 2003; Geissler et al., 2008). Accepting the phase identification at TDC-C with a relative delay of the P410s of more than four seconds implies very low S wave velocities directly beneath and slightly west of Tristan da Cunha. More difficult is the identification of the P660s, since we observe two phases around the predicted delay time of 68.1 s at TRIS-S. The first phase at 65.6 s would fit to a model with a shallower “660” due to a strong positive temperature anomaly in the mantle transition zone (about 40 km thinned), almost as strong as observed beneath Hawaii (Li et al., 2003; Woelbern et al., 2006). The noisier temporary data at TDC-C supports these observations extending the affected area at the mantle transition zone northwards beneath the hot spot islands. That would imply that a narrow (~100 to 150 km in diameter?) positive heat anomaly in the order of about +400 K (according to Woelbern et al., 2006) in the mantle transition zone to the west-south/southwest of Tristan da Cunha (see Fig. 10). This would be also in concordance with results from a teleseismic finite-frequency P wave tomography that

images a narrow low-velocity conduit in the upper mantle in the same area (Schloemer et al., in review by Earth and Planetary Science Letters). The second P660s phase could in that case be related to phase transformation of garnet (see Simmons and Gurrola, 2000), indicating that the mantle transition zone beneath the South Atlantic might also contain a significant non-olivine component. As tested by Woelbern et al. (2006), multiple phases from more shallow discontinuities can also disturb the observations at the mantle transition zone.

The potential existence of only a very narrow (~100 to 150 km in diameter?) mantle plume in the mantle transition zone would be in accord with data from the South Pacific Ocean, where also only narrow anomalies could be inferred at the mantle transition zone discontinuities by Niu et al. (2002) and Suetsugu et al. (2009) beneath some of the South Pacific hotspots. It is worth repeating that we cannot identify primary phases from the mantle transition zone with high confidence because of the limitations of the data set. Some arrivals might represent multiple converted or also scattered phases. Data observed at the OBS stations is even more sparse and noisy.

Base of lithosphere

Sp and SKSp receiver functions observe the base of the lithosphere at station TRIS at about 8 seconds lead time. Applying an empirical factor of 8.94 (e.g., Geissler et al., 2012), the lead time can be translated into depth. It is difficult to derive error estimates from the existing data, but we think that the uncertainties should be in the order of 0.5 to 1 seconds for the lead times and 5 to 10 km for depth, respectively. Therefore, the mean lithospheric thickness around Tristan da Cunha is about 70 to 75 km. This is slightly more than the 56 km thermal thickness expected from cooling of

normal oceanic lithosphere that has an age of about 26 Ma beneath Tristan da Cunha (see Humphreys and Niu, 2009). SKSp receiver functions observe the base of lithosphere closer to the stations since the incidence angle of the SKS phases is much steeper. The data analysed at different backazimuth ranges and filtered at 10 s low pass indicate a moderate thinning of the lithosphere beneath the island to about 6.8 s lead time (about 60 km depth), see Fig. 9. This might be caused by the thermal and magmatic overprinting due to hotspot activity.

Our depth estimates are in good agreement with the results obtained by the magnetotelluric experiment (see Baba et al., 2017). Baba et al. (2017) estimate the thickness of the lithosphere beneath the study area to be 60 to 70 km based on the 3D distribution of the electrical conductivity. Such a deep base of lithosphere beneath 26 Ma year old oceanic crust, especially beneath an active hot spot strongly argue for a compositional lithosphere beneath the oceans, following Morgan (1997), Hirth and Kohlstedt (1996), and Gaherty et al. (1996). That means that melt depletion and dehydration have a strong control on the depth of the regional seismological and also the electromagnetic lithosphere-asthenosphere boundary.

5. Conclusions

Analysing receiver functions from temporary ocean-bottom stations in the vicinity of the Tristan da Cunha hotspot, we do not find a significant thickening of the oceanic crust. The crustal thicknesses of 5.5 to 7.5 km around the hotspot are surprisingly homogenous and close to the global average of 7 km. This can be taken as evidence that there is no major contribution of a potential mantle plume heat and melt anomaly to the crustal production at the nearby mid-ocean ridge. A minor contribution or later thickening by plume-related magmatism in the order of 0.5 to 1 km cannot be ruled

out. The crustal thickness beneath and close to the islands indicate also only minor overprint by the hotspot, but there might be a more complicated Moho structure beneath Nightingale Island due to ongoing magmatic processes (see also Weit et al., in press).

From the Ps receiver functions, we do not have clear observations of the base of the lithosphere. The crustal multiples might mask weak converted phases from the lithosphere-asthenosphere boundary. There are indications for a low velocity zone in the upper mantle beneath station TRIS. Sp and SKSp receiver functions observed at station TRIS image the base of lithosphere at about 60 to 75 km depth. This depth is in accordance with the results from the magnetotelluric study (Baba et al., 2017) and argues for a compositional oceanic lithosphere beneath the study area.

Studying the P410s and P660s converted phases, we can exclude a major thermal imprint of a hot mantle plume in the mantle transition zone west/northwest of Tristan da Cunha towards the Mid-Atlantic ridge. There are indications but not clear evidence for hot material penetrating the mantle transition zone to the south of the Tristan da Cunha hotspot.

Our findings will help to better constrain geodynamic models of the South Atlantic (Gassmoeller et al., 2016).

Acknowledgements

We thank the captain Ralf Schmidt, the crew of R/V Maria S. Merian and the Scientific Parties of cruise MSM20/2 and MSM24 as well as the people on Tristan da Cunha for the professional and friendly support. Furthermore, we thank two anonymous reviewers for their constructive criticism. Figures were produced using Generic Mapping Tools (Wessel et al., 2013). This work was supported by the

German Research Foundation (DFG) grant GE 1783/4-1/2 as part of the Priority Program SPP1375. Additional support was provided by the Alfred Wegener Institute Bremerhaven. Instruments were provided by "Deutscher Geräte-Pool für Amphibische Seismologie (DEPAS)" at Alfred Wegener Institute Bremerhaven and Deutsches Geoforschungszentrum Potsdam.

References

Anderson, D.L., 2005. Scoring hotspots: the plume and plate paradigms. Geol. Soc. Special Papers 388, 31–54.

Baba, K., Chen, J., Sommer, M., Utada, H., Geissler, W.H., Jokat, W., Jegen, M., in press. Marine magnetotellurics imaged no distinct plume beneath the Tristan da Cunha hotspot in the southern Atlantic Ocean. Tectonophysics, doi:http://dx.doi.org/10.1016/j.tecto.2016.09.033.

Birch, F., 1961. The velocity of compressional waves in rocks to 10 kilobars (Part II). J. Geophys. Res. 65, 1083–1102.

Bock, G., 1991. Long-period S to P converted waves and the onset of partial melting beneath Oahu, Hawaii. Geophysical Research Letters 18(5), 869-872, doi:10.1029/91GL01055.

Courtillot, V., Davaille, A., Besse, J., Stock, J., 2003. Three distinct types of hotspots in the Earth's mantle. Earth and Planetary Science Letters 205(3–4), 295-308, doi:http://dx.doi.org/10.1016/S0012-821X(02)01048-8.

French, S.W., Romanowicz, B., 2015. Broad plumes rooted at the base of the Earth's mantle beneath major hotspots. Nature 525(7567), 95-99, doi:10.1038/nature14876.

Fuchs, K., Müller, G., 1971. Computation of synthetic seismograms with the reflectivity method and comparison with observations. Geophys. J. Roy. Astron. Soc. 21, 261 – 283.

Gaherty, J.B., Jordan, Y.H., Gee, L.S., 1996. Seismic structure of the upper mantle in a central Pacific corridor. Journal of Geophysical Research: Solid Earth,101(B10), 22291-22309, doi:10.1029/96JB01882.

Gassmöller, R., Dannberg, J., Bredow, E., Steinberger, B., Torsvik, T.H., 2016. Major influence of plume-ridge interaction, lithosphere thickness variations, and global mantle flow on hotspot volcanism—The example of Tristan. Geochemistry, Geophysics, Geosystems 17(4), 1454-1479, doi:10.1002/2015GC006177.

Geissler, W.H., 2014. Electromagnetic, gravimetric and seismic measurements to investigate the Tristan da Cunha hot spot and its role in the opening of the South Atlantic Ocean (MARKE) - Cruise No. MSM24 - December 27, 2012 - January 21, 2013 - Walvis Bay (Namibia) - Cape Town (South Africa), 1-56; MARIA S. MERIAN-Berichte, DFG-Senatskommission für Ozeanographie, Bremen, doi:10.2312/cr_msm24

Geissler, W.H., Kind, R., Yuan, X., 2008. Upper mantle and lithospheric heterogeneities in central and eastern Europe as observed by teleseismic receiver functions. Geophysical Journal International 174(1), 351-376, doi:10.1111/j.1365-246X.2008.03767.x.

Geissler, W.H., Kämpf, H., Skácelová, Z., Plomerová, J., Babuška, V., Kind, R., 2012. Lithosphere structure of the NE Bohemian Massif (Sudetes) — A teleseismic receiver function study. Tectonophysics 564–565, 12-37, doi:http://dx.doi.org/10.1016/j.tecto.2012.05.005.

Gibson, S.A., Thompson, R.N., Day, J.A., 2006.Timescales and mechanisms of plume–lithosphere interactions: 40Ar/39Ar geochronology and geochemistry of alkaline igneous rocks from the Paraná–Etendeka large igneous province. Earth and Planetary Science Letters 251(1–2), 1-17, doi:http://dx.doi.org/10.1016/j.epsl.2006.08.004.

Gu, Y.J., Dziewonski, A.M., 2002. Global variability of transition zone thickness, Journal of Geophysical Research: Solid Earth 107(B7), ESE 2-1-ESE 2-17, doi:10.1029/2001JB000489.

Helffrich, G., 2000. Topography of the transition zone seismic discontinuities, Reviews of Geophysics 38(1), 141-158.

Hirth, G., Kohlstedt, D.L., 1996. Water in the oceanic upper mantle: implications for rheology, melt extraction and the evolution of the lithosphere. Earth Planet. Sci. Lett. 144, 93-108.

Humphreys, E.R., Niu, Y., 2009. On the composition of ocean island basalts (OIB): The effects of lithospheric thickness variation and mantle metasomatism. Lithos 112(1-2), 118-136, doi:10.1016/j.lithos.2009.04.038.

Jokat, W., Stefanie Kessling, S. (2017). Hotspot volcanism in the southern South Atlantic: Geophysical constraints on the evolution of the southern Walvis Ridge and the Discovery Seamounts, Tectonophysics, accepted.

Kennett, B.L.N., 1991. IASP 1991 Seismological Tables, Research School of Earth Sciences, Australian National University, Canberra, Australia.

Kind, R., 1985. The reflectivity method for different source and receiver structures and comparison with GRF data. J. Geophys. 58, 146–152.

Kind, R., Kosarev, G.L., Petersen, N.V., 1995. Receiver functions at the stations of the German Regional Seismic Network (GRSN). Geophysical Journal International 121, 191–202.

Kumar, P., Kawakatsu, H.,2011. Imaging the seismic lithosphere-asthenosphere boundary of the oceanic plate. Geochemistry Geophysics Geosystems 12(1), doi:10.1029/2010gc003358.

Kumar, P., Kawakatsu, H., Shinohara, M., Kanazawa, T., Araki, E., Suyehiro, K., 2011. P and Sreceiver function analysis of seafloor borehole broadband seismic data. Journal of Geophysical Research 116(B12), doi:10.1029/2011jb008506.

Leahy, G.M., Collins, J.A., Wolfe, C.J., Laske, G., Solomon, S.C., 2010. Underplating of the Hawaiian Swell: evidence from teleseismic receiver functions. Geophysical Journal International 183(1), 313-329, doi:10.1111/j.1365-246X.2010.04720.x.

Lebedev, S., Chevrot, S., van der Hilst, R.D., 2002. Seismic Evidence for Olivine Phase Changes at the 410- and 660-Kilometer Discontinuities. Science 296, 1300-1302.

Lebedev, S., van der Hilst, R.D., 2008. Global upper-mantle tomography with the automated multimode inversion of surface and S-wave forms. Geophysical Journal International,173(2), 505-518, doi:10.1111/j.1365-246X.2008.03721.x.

Li, X., Kind, R., Priestley, K., Sobolev, S.V., Tilmann, F., Yuan, X., Weber, M., 2000. Mapping the Hawaiian plume conduit with converted seismic waves. Nature 405, 938-941.

Li, X., Kind, R.,Yuan, X., 2003. Seismic study of upper mantle and transition zone beneath hotspots. Physics of the Earth and Planetary Interiors 136(1-2), 79-92, doi:10.1016/s0031-9201(03)00021-9.

Morgan, W.J., 1971. Convection Plumes in the Lower Mantle. Nature 230(5288), 42-43.

Morgan, J.P., 1997. The generation of a compositional lithosphere by mid-ocean ridge melting and its effect on the subsequent off-axis hotspot upwelling and melting. Earth Planet. Sci. Lett. 146, 213-232.

Müller, R.D., Sdrolias, M., Gaina, C., Roest, W.R., 2008. Age, spreading rates and spreading symmetry of the world's ocean crust. Geochem. Geophys. Geosyst. 9, Q04006, doi:10.1029/2007GC001743.

Niu, F., Solomon, S.C., Silver, P.G., Suetsugu, D., Inoue, H., 2002. Mantle transition-zone structure beneath the South Pacific Superswell and evidence for a mantle plume underlying the Society hotspot. Earth and Planetary Science Letters 198, 371-380.

O'Connor, J.M., Duncan, R.A., 1990. Evolution of the Walvis Ridge-Rio Grande Rise Hot Spot System: Implications for African and South American Plate motions over plumes. Journal of Geophysical Research: Solid Earth 95(B11), 17475-17502, doi:10.1029/JB095iB11p17475.

O'Connor, J.M., Jokat, W., le Roex, A.P., Class, C., Wijbrans, J.R., Keszling, S., Kuiper, K.F., Nebel, O., 2012. Hotspot trails in the South Atlantic controlled by plume and plate tectonic processes. Nature Geosci 5(10), 735-738.

Parsons, B., Sclater, J.G., 1977. An analysis of the variation of ocean floor bathymetry and heat flow with age. Journal of Geophysical Research 82(5), 803-827, doi:10.1029/JB082i005p00803.

Rohde, J. K., van den Bogaard, P., Hoernle, K., Hauff, F., Werner, R., 2013. Evidence for an age progression along the Tristan-Gough volcanic track from new

40Ar/39Ar ages on phenocryst phases. Tectonophysics 604, 60-71, doi:10.1016/j.tecto.2012.08.026.

Schloemer, A., Geissler, W.H., Jokat, W., Jegen, M., Hunting for the Tristan Mantle Plume - An upper mantle tomography around the volcanic island of Tristan da Cunha. Earth Planet. Sci. Lett., in review.

Simmons, N.A., Gurrola, H., 2000. Multiple seismic discontinuities near the base of the transition zone in the Earth's mantle. Nature 405(6786), 559-562.

Suetsugu, D., Shinohara, M., Araki, E., Kanazawa, T., Suyehiro, K., Yamada, T., Nakahigashi, K., Shiobara, H., Sugioka, H., Kawai, K., Fukao, Y., 2005. Mantle discontinuity depths beneath the West Philippine Basin from receiver function analysis of deep-sea borehole and seafloor broadband waveforms. Bull. Seismol. Soc. Am. 95, 1947–1956, doi:10.1785/0120040169.

Suetsugu, D., Isse, T., Tanaka, S., Obayashi, M., Shiobara, H., Sugioka, H.,Kanazawa, T., Fukao, Y., Barruol, G., Reymond, D., 2009. South Pacific mantle plumes imaged by seismic observation on islands and seafloor. Geochemistry, Geophysics, Geosystems 10(11), Q11014, doi:10.1029/2009gc002533.

Vinnik, L.P., 1977. Detection of waves converted from P to SV in the mantle. Physics of the Earth and Planetary Interiors 15(1), 39-45, doi:http://dx.doi.org/10.1016/0031-9201(77)90008-5.

Wang, R., 1999. A simple orthonormalization method for stable and efficient computation of Green's functions. Bulletin of the Seismological Society of America 89(3), 733-741.

Weit, A., Trumbull, R.B., Keiding, J.K., Geissler, W.H., Gibson, S.A., Veksler, I.V., in press. The magmatic system beneath the Tristan da Cunha Island: Insights from

thermobarometry, melting models and geophysics. Tectonophysics, doi:http://dx.doi.org/10.1016/j.tecto.2016.08.010.

Wessel, P., Smith, W.H.F., Scharroo, R., Luis, J., Wobbe F., 2013. Generic Mapping Tools: improved version released. Eos, Trans. AGU 94(45), 409–420.

White, R.S., McKenzie, D., O'Nions, R.K.,1992. Oceanic crustal thickness from seismic measurements and rare earth element inversions. Journal of Geophysical Research: Solid Earth 97(B13), 19683-19715, doi:10.1029/92JB01749.

Wölbern, I., Jacob, A.W.B., Blake, T.A., Kind, R., Li, X., Yuan, X., Duennebier, F., Weber, M., 2006. Deep origin of the Hawaiian tilted plume conduit derived from receiver functions. Geophysical Journal International 166(2), 767-781, doi:10.1111/j.1365-246X.2006.03036.x.

Yuan, X., Ni, J., Kind, R., Mechie, J., Sandvol, E., 1997. Lithospheric and upper mantle structure of southern Tibet from a seismological passive source experiment. Journal of Geophysical Research 102 (B12), 27,491–27,500.

Yuan, X., Asch, G., Bataille, K., Bock, G., Bohm, M., Echtler, H., Kind, R., Oncken, O., Wölbern, I., 2006a. Deep seismic images of the Southern Andes. In: Kay, S. M., Ramos, V. A. (Eds.), *Evolution of an Andean margin: A Tectonic and Magmatic View from the Andes to the Neuquén Basin (35°–39°S lat)*, (Special Paper / Geological Society of America Special; 407), pp. 61—72. DOI: http://doi.org/10.1130/2006.2407(03)

Yuan, X., Kind, R., Li, X., Wang, R., 2006b. The S receiver functions: synthetics and data example. Geophysical Journal International 165 (2), 555–564.

Zandt, G., Myers, S.C., Wallace, T.C., 1995. Crust and mantle structure across the Basin and Range-Colorado Plateau boundary at 37°N latitude and implications for

Cenozoic extensional mechanism. Journal of Geophysical Research: Solid Earth 100(B6), 10529-10548, doi:10.1029/94JB03063.

Zhu, L., Kanamori, H., 2000. Moho depth variation in southern California from teleseismic receiver functions. Journal of Geophysical Research: Solid Earth 105(B2), 2969-2980, doi:10.1029/1999JB900322.

Tables

Table 1

Coordinates of stations, orientation of XY components, delay Times of Moho converted phases, crustal thicknesses, Vp/Vs ratios (see xls file). Values taken for calculation of crustal thicknesses in Fig. 9 are marked in bold. Sparse, more noisy or unclear observations are marked in cursive

t_{Ps}, Ps delay time; t_{PpPs}, PpPs delay time; $t_{PsPs+PpSs}$, PsPs+PpSs delay time; Δt, maximum difference in PsPs+PpSs delay times between the observations for low pass of 2 s, 3 s and 5 s; H, crustal thickness; LP, low pass corner frequency; n, number of stacked traces.

Table 2. Delay times of P410s and P660s converted phases. Unambiguous and therefore most reliable observations are marked in bold. Observations with higher uncertainty are marked in cursive.

t_{P410s}, Ps delay time from 410 km conversion; t_{P660s}, Ps delay time from 660 km conversion; dt, differential delay time for mantle transition zone conversions; n, number of stacked traces.

Table 3. Lead times of Sp and SKSp converted phases for intra-lithospheric discontinuities and base of lithosphere. Observations used for interpretation are marked in bold. Observations with higher uncertainty are marked in cursive. n, number of events. (see xls file)

BAZ, back azimuth; t_{SMp}, Sp lead time Moho and/or shallow lithosphere; t_{SLABp}, Sp lead time lithosphere-asthenosphere boundary; n, number of stacked traces.

Figure captions

Figure 1: Seismological station distribution. Gray dashed lines indicate the age of the underlying lithosphere (Mueller et al., 2008). There are no three-component data available from stations marked by gray or white triangles. Colour bar, ETOPO2 bathymetry. Inset: Position of the study area within the South Atlantic. EP, Etendeka Plateau; GI, Gough Island; TDCI, Tristan da Cunha Islands, MAR, Mid-Atlantic Ridge; WR, Walvis Ridge.

Figure 2

Stacked receiver functions for different period ranges at selected stations. a) permanent observatory TRIS on Tristan da Cunha; b) temporary station NIG01 on Nightingale Island; c) stacks of all OBS traces; d) OBS station TDC26. Phases discussed in the text are marked by coloured dashed lines. Please note the negative phase at around 3 to 6 s delay time (red marked), which we interpret as the 2nd multiple from the crust-mantle boundary (Moho).

Figure 3: Stacking results in the Vp/Vs-Depth domain (Zhu and Kanamori 2000) for a) station TRIS (period range 3 s to 20 s), b) all OBS traces (period range 2s to 20 s). The dark grey areas mark high amplitudes. The white boxes mark the absolute stacked maximum, which was found by grid search within the intervals of 3 to 12 km for the Moho depth and 1.50 to 2.00 for the Vp/Vs ratio. An average crustal P-wave velocity of 6.0 km/s was assumed. The surrounding ellipses mark the regions between 95% and 99% of the maximal stacked amplitude with 1% interval. The half-width of the 95% region gives an estimate of the uncertainty of the method.

Figure 4: Stacked receiver functions for all OBS/land stations at two selected period ranges. a) period range 2 s to 20 s; b) period range 3 s to 20 s. Stations are sorted according to the age of the underlying lithosphere (see Fig. 1). Consistent phases are marked by blue and yellow (positive polarity), and red (negative polarity) dashed lines. Further period ranges are shown in Appendix 2.

Figure 5: Observations from the mantle transition zone. Vertical lines mark the theoretical arrival times of the P410s and P660s. a) Ps receiver functions at station TRIS in different period ranges; b) Stacks of all OBS traces in different period ranges; c) Ps receiver functions at station TRIS in the period range 7 s to 50 s for different backazimuth sectors and moveout correction for primary and multiple converted phases. The piercing points at 410 and 660 km depth are mapped in Fig. 10; d) Ps receiver functions observed at temporary OBS stations and at station NIG01 in the period range 7 s to 20 s. The individual traces were stacked in subsets according to their piercing points in 410 km depth (see Fig. 10) Stacks with correction for different moveout for primary and multiple converted phases are shown.

Figure 6: Stacks of synthetic receiver functions for a 7 km thick one layer oceanic crust with (M3) and without (M4) a 3 km thick water layer.

Figure 7: Forward modelling of crustal and upper mantle structure to constrain the phase interpretations. a) OBS station TDC26. The simple crustal model is able to explain the first 5 s of the observed waveform. b) station TRIS. The simple crustal model is able to explain the first 10 s of the observed waveform. c) station NIG01. A simple 6 km thick crust (black lines) can explain the first 5 s of the observed waveform. Introducing a Moho at 18 km depth would fit the observed minimum at ~10 s delay time (red lines). A reasonable fit of the first 12 s of the observed waveform can be achieved by a complex crust-mantle transition zone between 6 and 18 km depth (blue lines). d) station TRIS. A sharp LAB at 45.5 km depth produce a negative multiple arrival at ~16 s delay time (red lines). Alternatively, a low velocity layer at 140 to 150 km depth can explain the positive and negative arrivals at ~16 s delay time (black lines). The smooth LAB at 50 to 65 km depth has only a minor effect on the amplitudes and cannot explain the negative phase at 6 s delay time.

Figure 8: Observation from the lithosphere-asthenosphere boundary. a) complete Sp, SKSp and Sp+SKSp receiver function stacks for station TRIS in two period ranges. b) Sp and and SKSp receiver function stacks in selected backazimuth ranges. The grey vertical dashed lines mark the converted phase from the base of lithosphere.

Figure 9: Map of crustal thickness calculated from the delay time of the 2nd multiple (PpsS+PspS) for the period range 2 s to 20 s. In case of the two island stations

(orange) their topography is corrected by 3.5 km (TRIS) and 3 km (NIG) respectively. The numbers with gray background are calculated a period range of 5 s to 20 s. Cursive numbers indicate stations at which observations are more noisy and sparse. The uncertainties are calculated based on the Ps delay time difference between different period ranges (see Tab. 1).

Inset: Sp and SKSp piercing points and lithosphere thicknesses around station TRIS as observed at stacks for different backazimuth ranges (see Fig. 8 for data). The lead times listed in Table 3 can be translated into depth by a factor of 8.94. The base of lithosphere is at about 60 to 72 km depth.

Figure 10: 3D sketch to summarize observation from the mantle transition zone discontinuities at 410 and 660 km depth. Ps piercing points for TRIS at 410 km (black crosses) and 660 km depth (red crosses). Individual receiver functions were stacked according to their piercing points at 410 km depth, see figures 5 and 6 for data. MAR, Mid-Atlantic Ridge; MTZ, mantle transition zone; TFZ, Tristan da Cunha fracture zone.

Captions for Appendices

Appendix 1

Stacked receiver functions for different period ranges for single stations and subset of stations (see Table 1). Phases discussed in the text are marked by coloured dashed lines. Please note the negative phase at around 3 to 6 s delay time (red marked), which we interpret as the 2nd multiple from the crust-mantle boundary (Moho).

Appendix 2

Stacked receiver functions for all OBS/land stations at two selected period ranges. a) period range 5 s to 20 s; b) period range 7 s to 20 s. Stations are sorted according to the age of the underlying lithosphere (see Fig. 1). Consistent phases are marked by blue and yellow (positive polarity), and red (negative polarity) dashed lines.

Appendix 3

a) station TRIS. Receiver function stacks for period bands 7 to 50 seconds and 10 to 50 seconds for P and PP primary phases separately and together. Please note that the primary P and PP phases arrive from different backazimuths. b) Stacks of all receiver functions observed at OBS stations and NIG01 for period bands 7 to 30 seconds and 10 to 30 seconds with moveout correction for primary and multiple converted phases. Traces for TRIS at 10 s to 50 seconds are shown for comparison.

Appendix 4

Ps receiver functions at station TRIS in the period range 7 s to 50 s for different backazimuth sectors. The piercing points at 410 and 660 km depth are mapped in Fig. 10.

Appendix 5

Ps receiver functions observed at temporary OBS stations and at station NIG01 in the period range 7 s to 20 s. The individual traces were stacked according to their piercing points in 410 km depth (see Fig. 10).

Appendix 6

Parameters of seismic velocity models used to calculate synthetic receiver functions (see Fig. 6). Qp and Qs are the seismic attenuation values for P and S waves, respectively.

Appendix 7

Velocity models used for modeling of receiver functions (see Fig. 7). n, number of sub-layers

Appendix 8

Sp and SKSp receiver functions for station TRIS for selected backazimuth ranges. The red vertical bars mark the converted phase from the base of lithosphere.

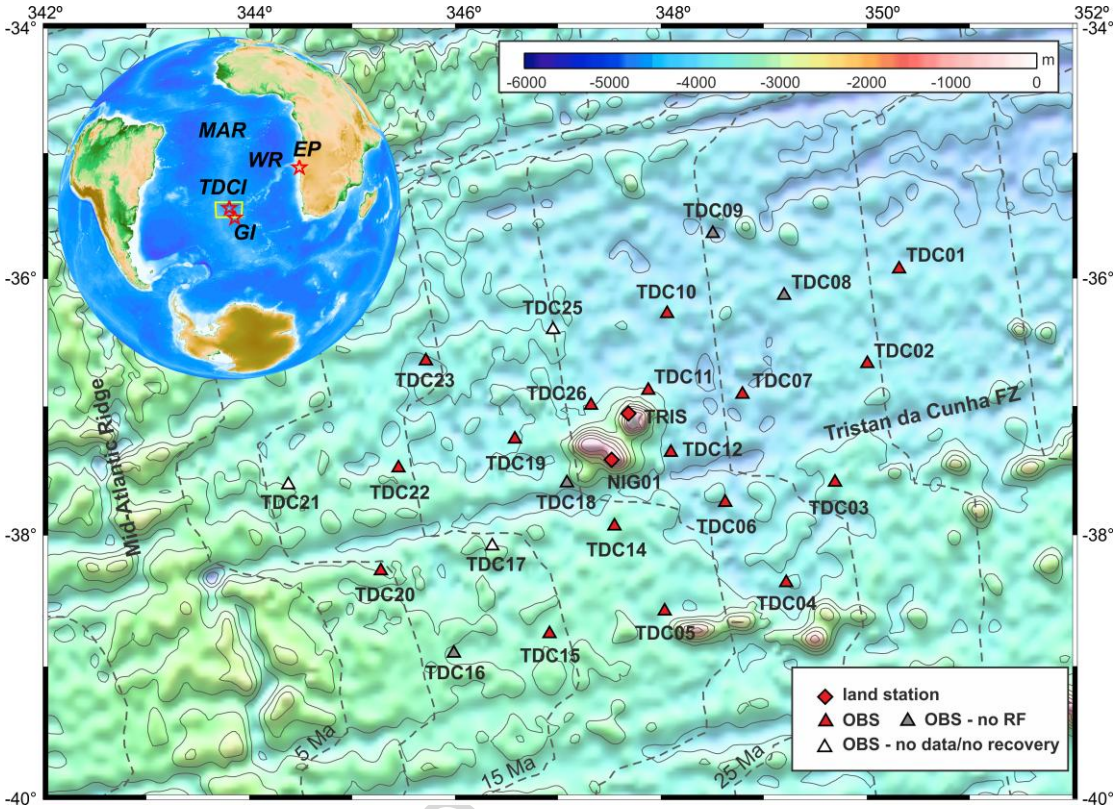

Fig. 1

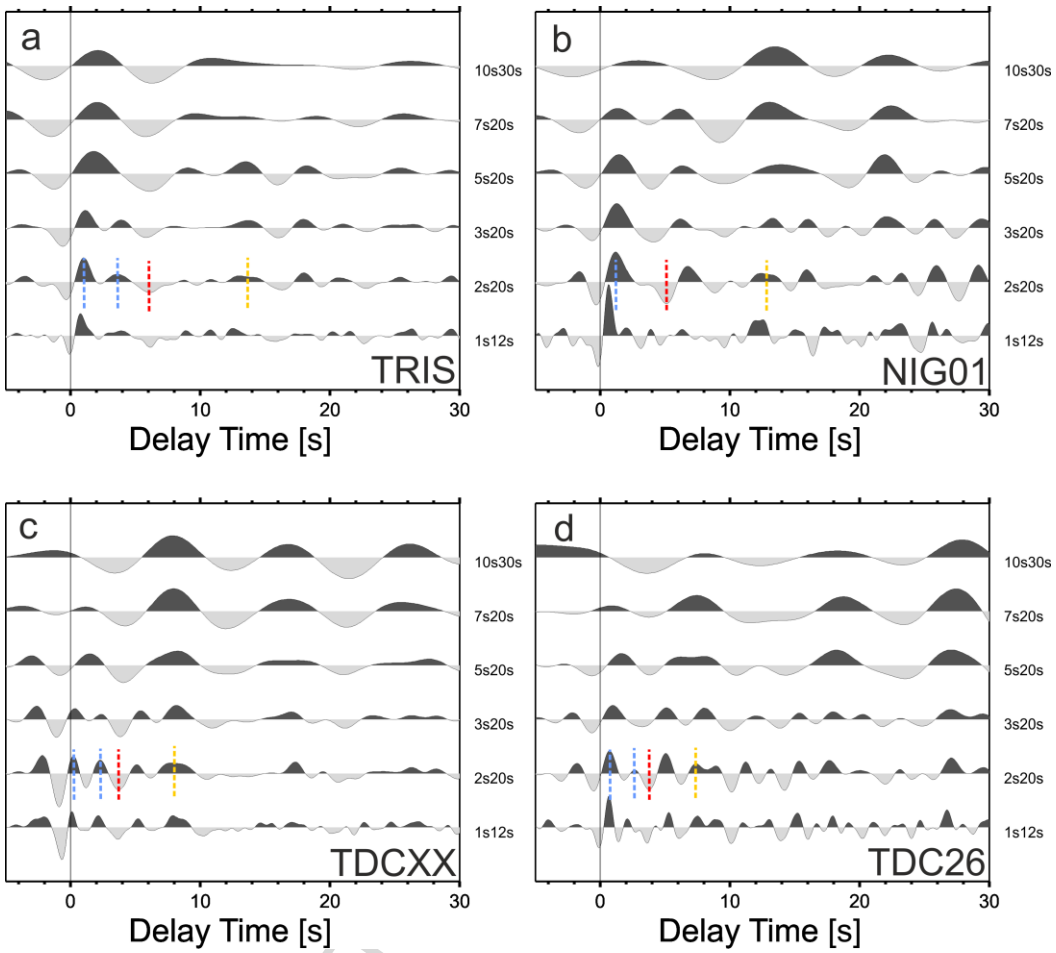

Fig. 2

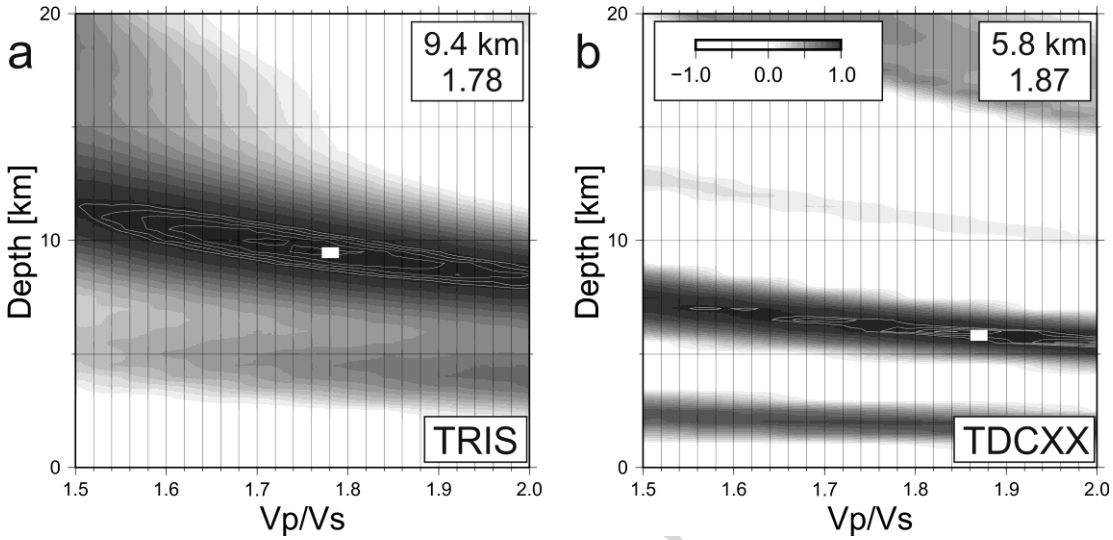

Fig. 3

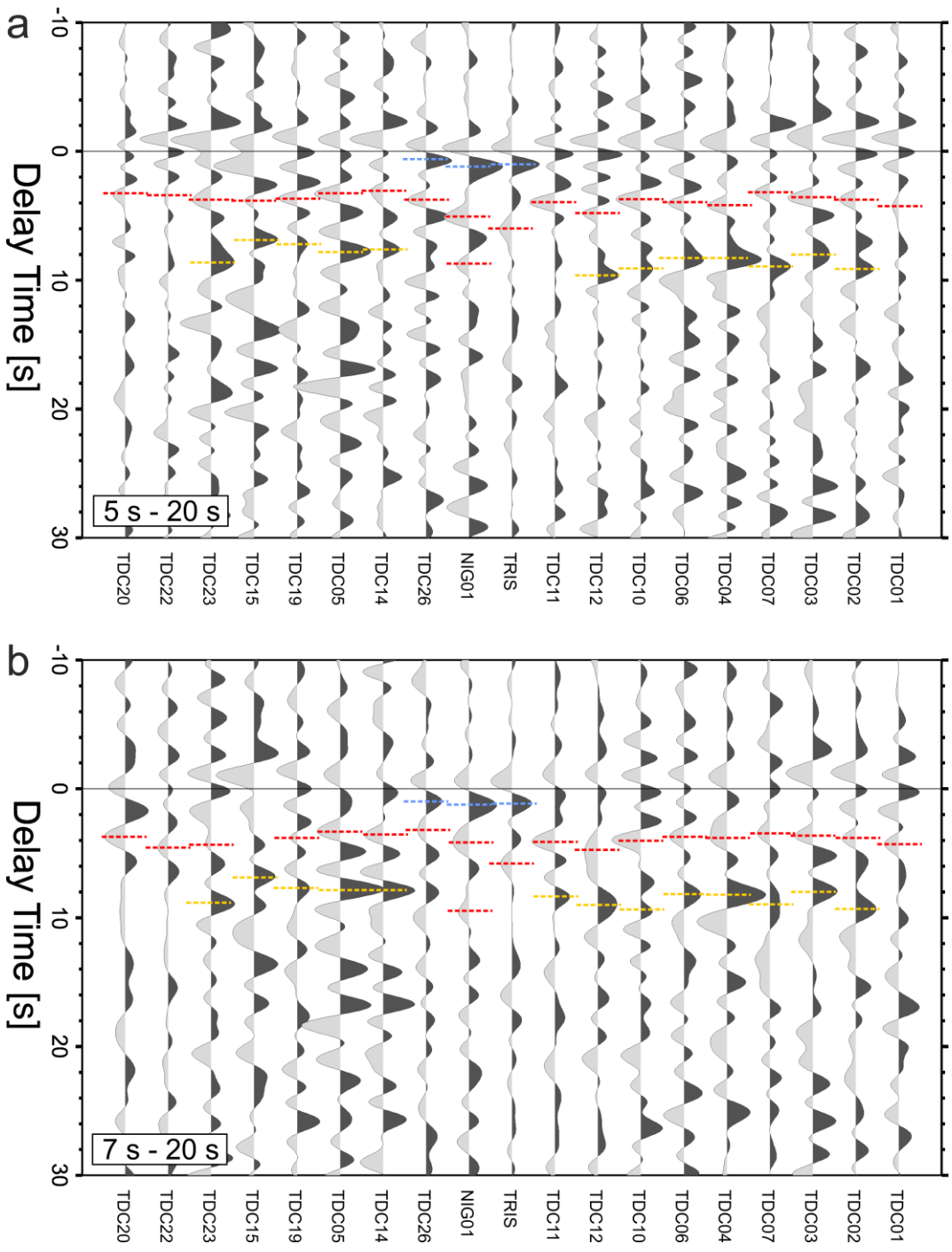

Fig. 4

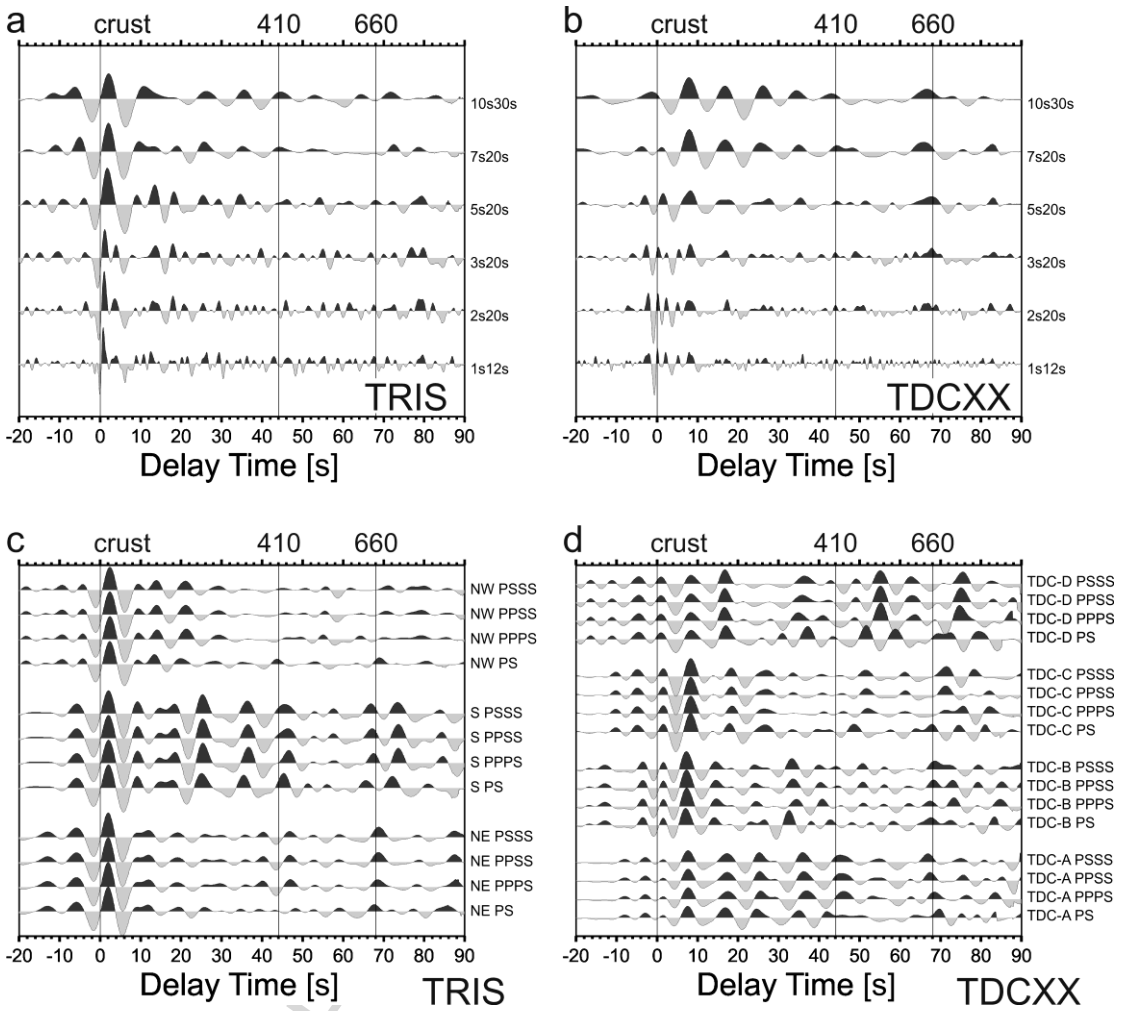

Fig. 5

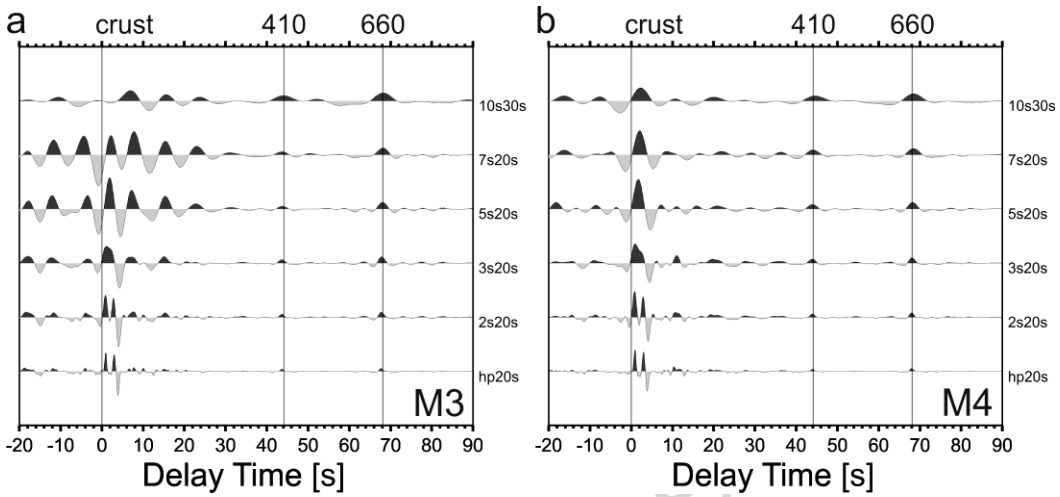

Fig. 6

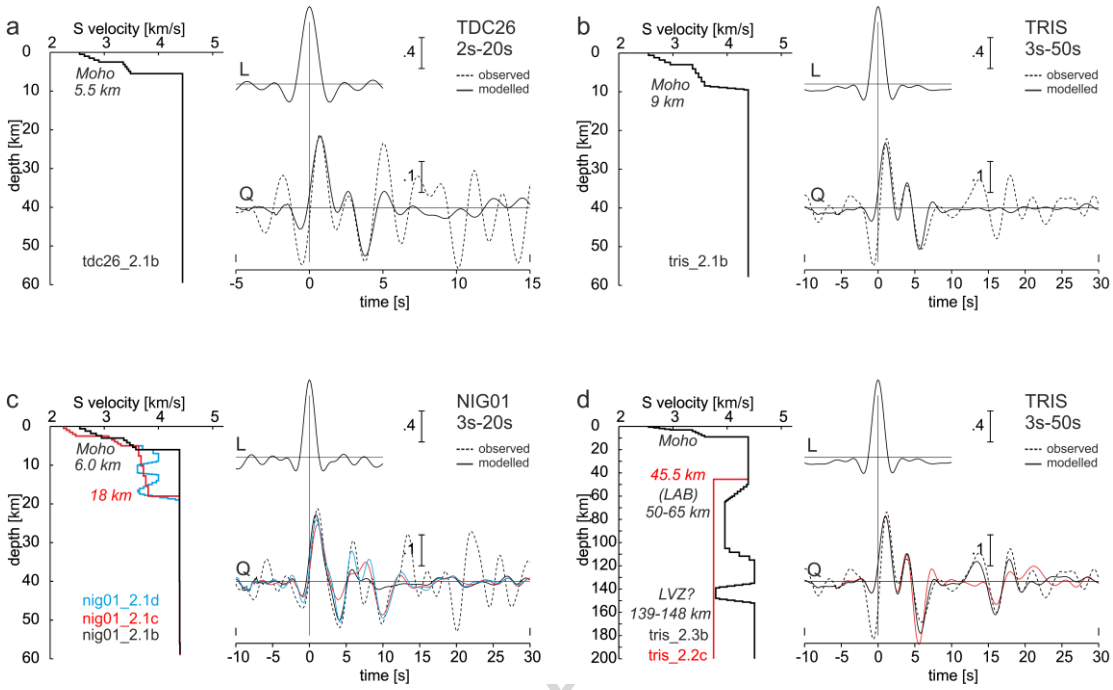

Fig. 7

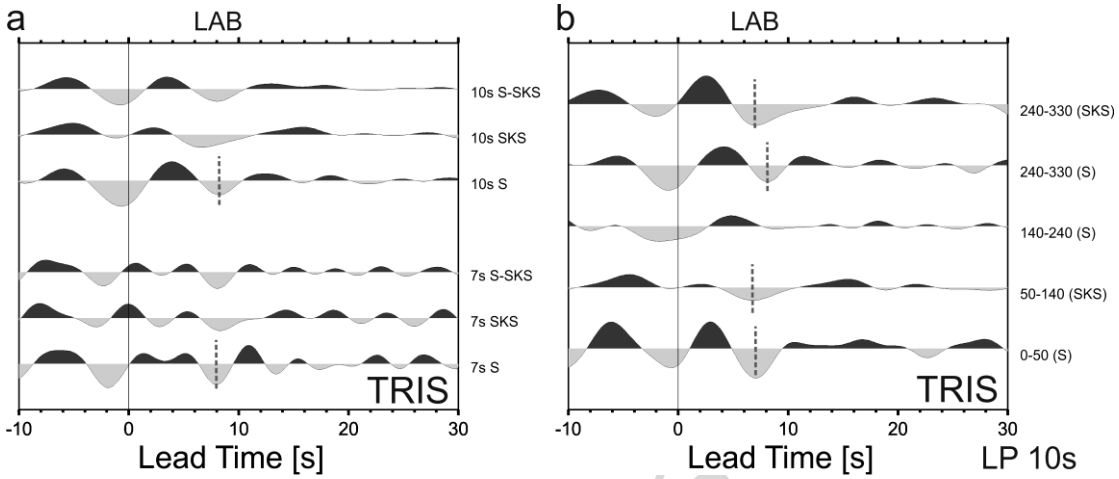

Fig. 8

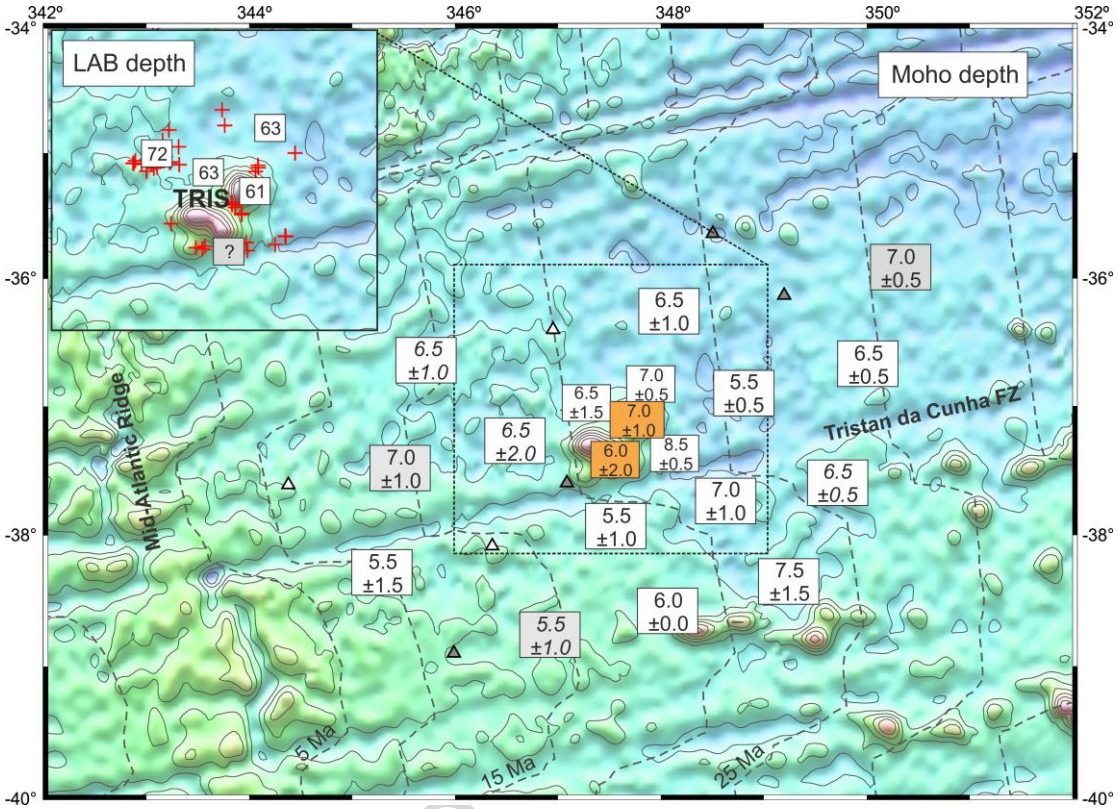

Fig. 9

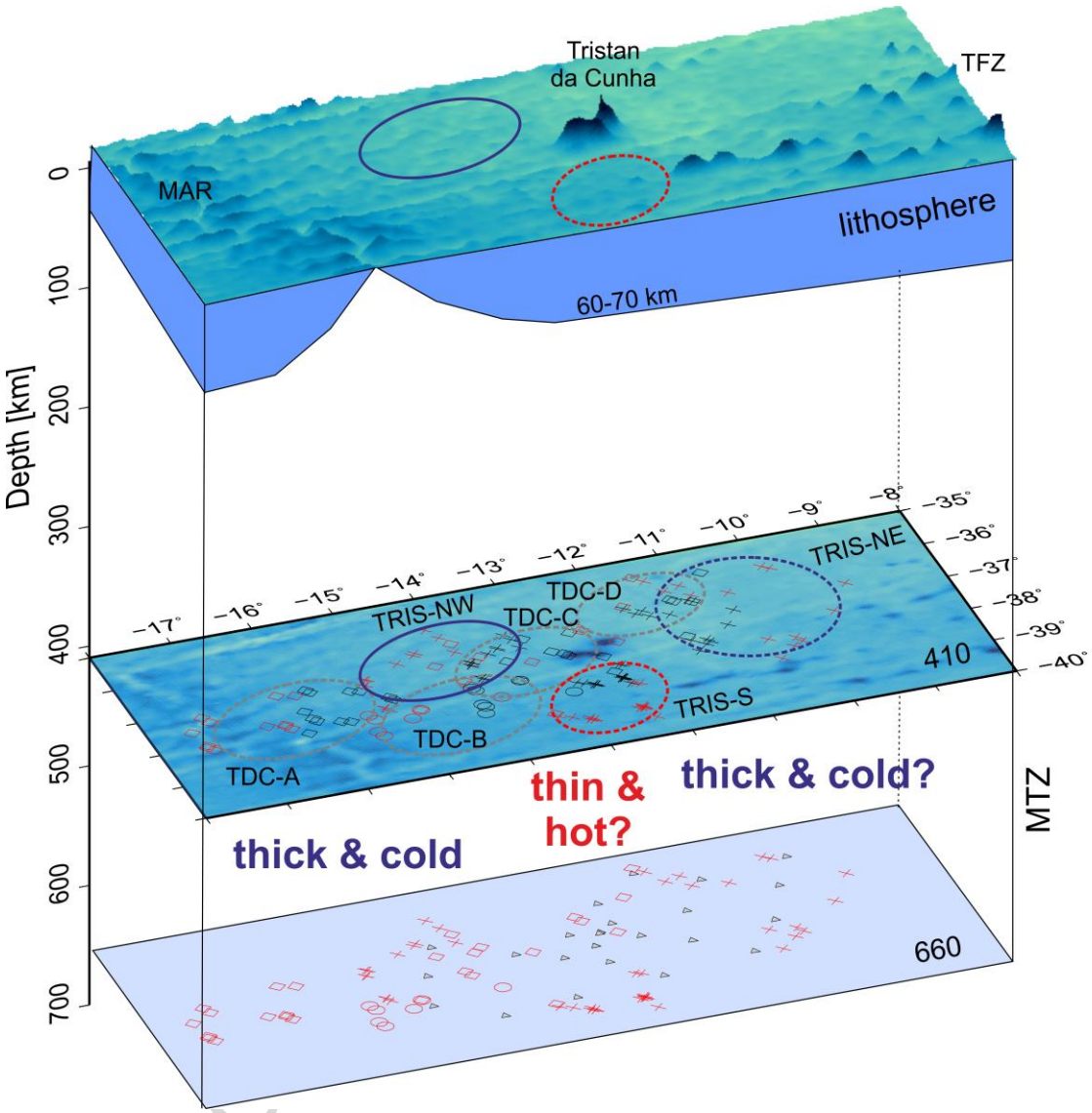

Fig. 10

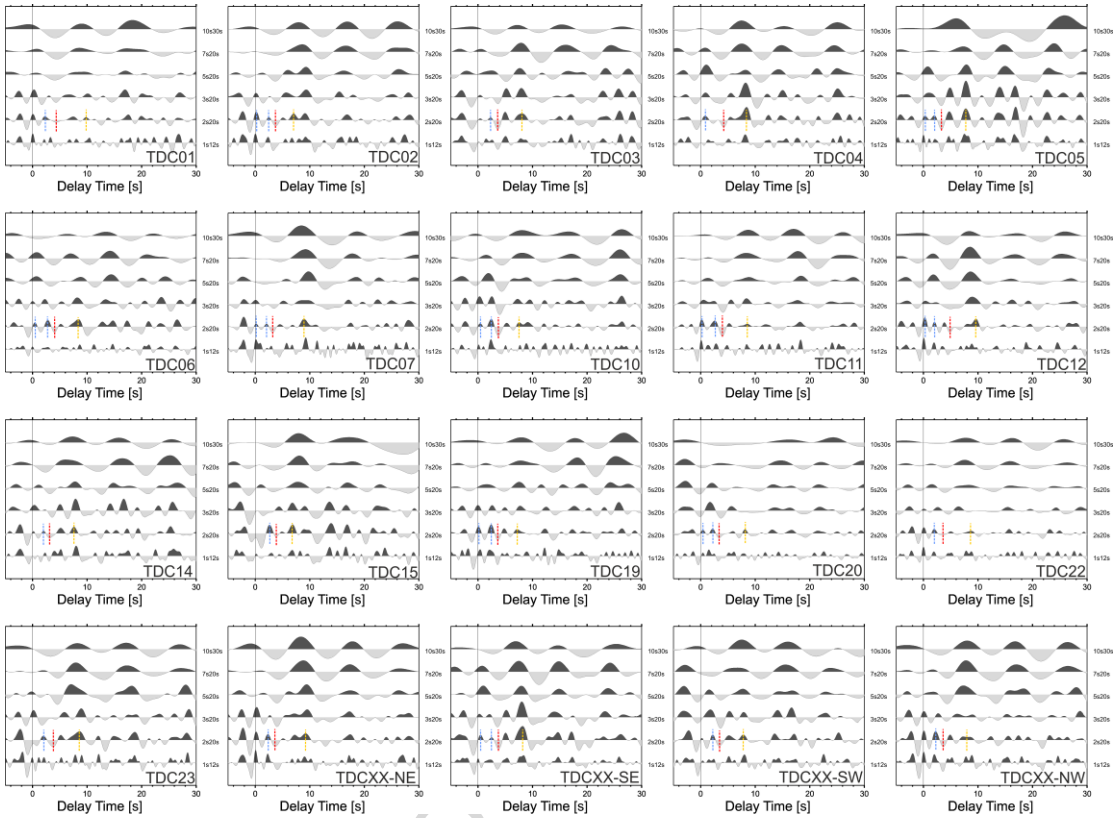

Appendix 1

Appendix 2

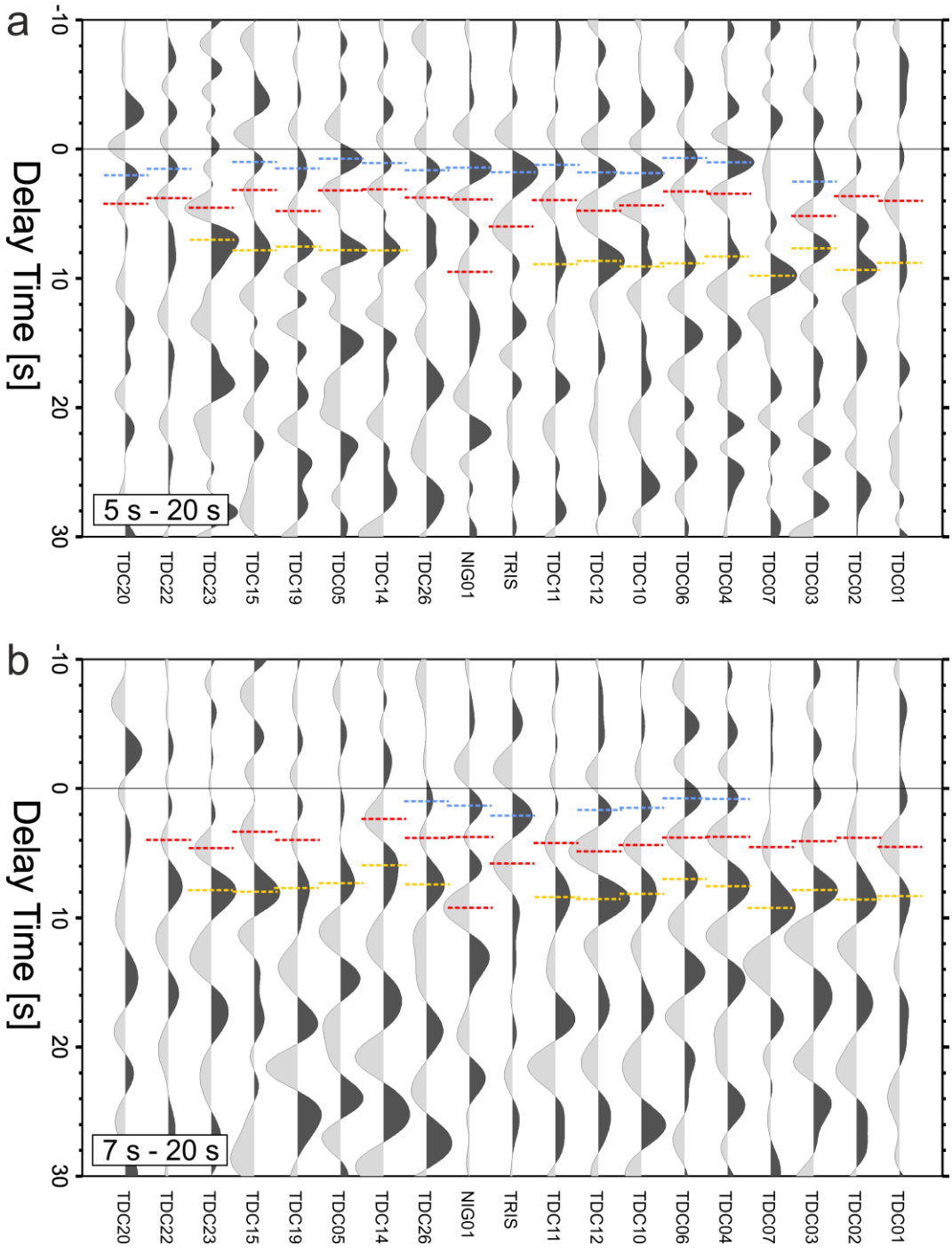

Appendix 3

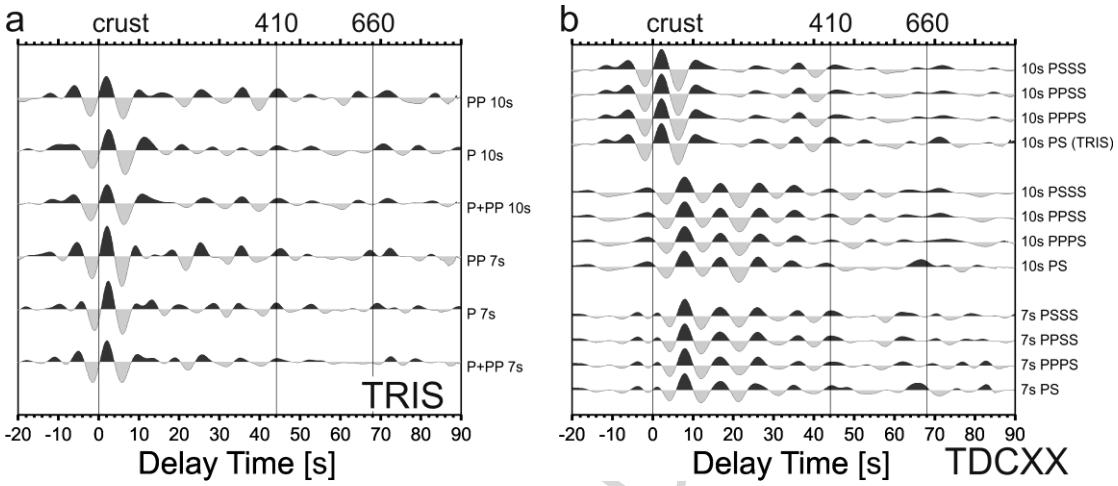

Appendix 4

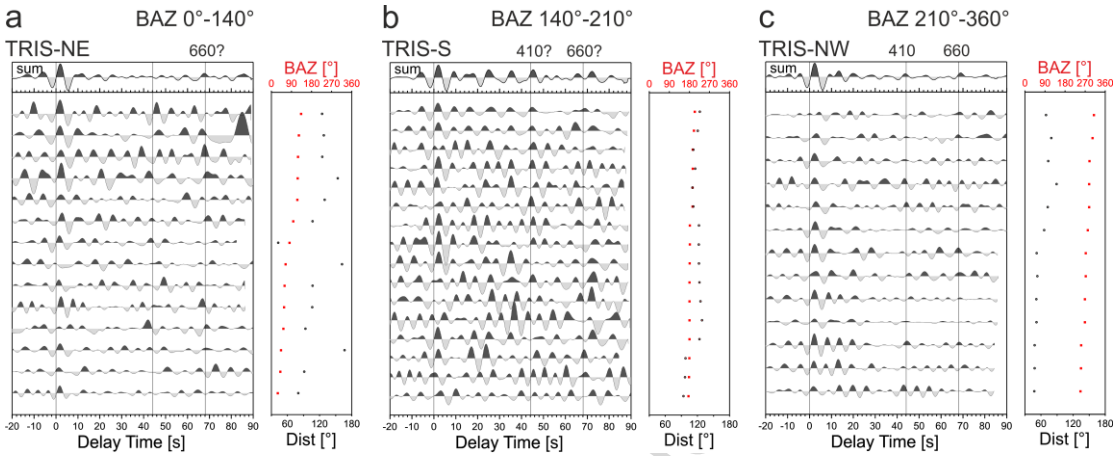

Appendix 5

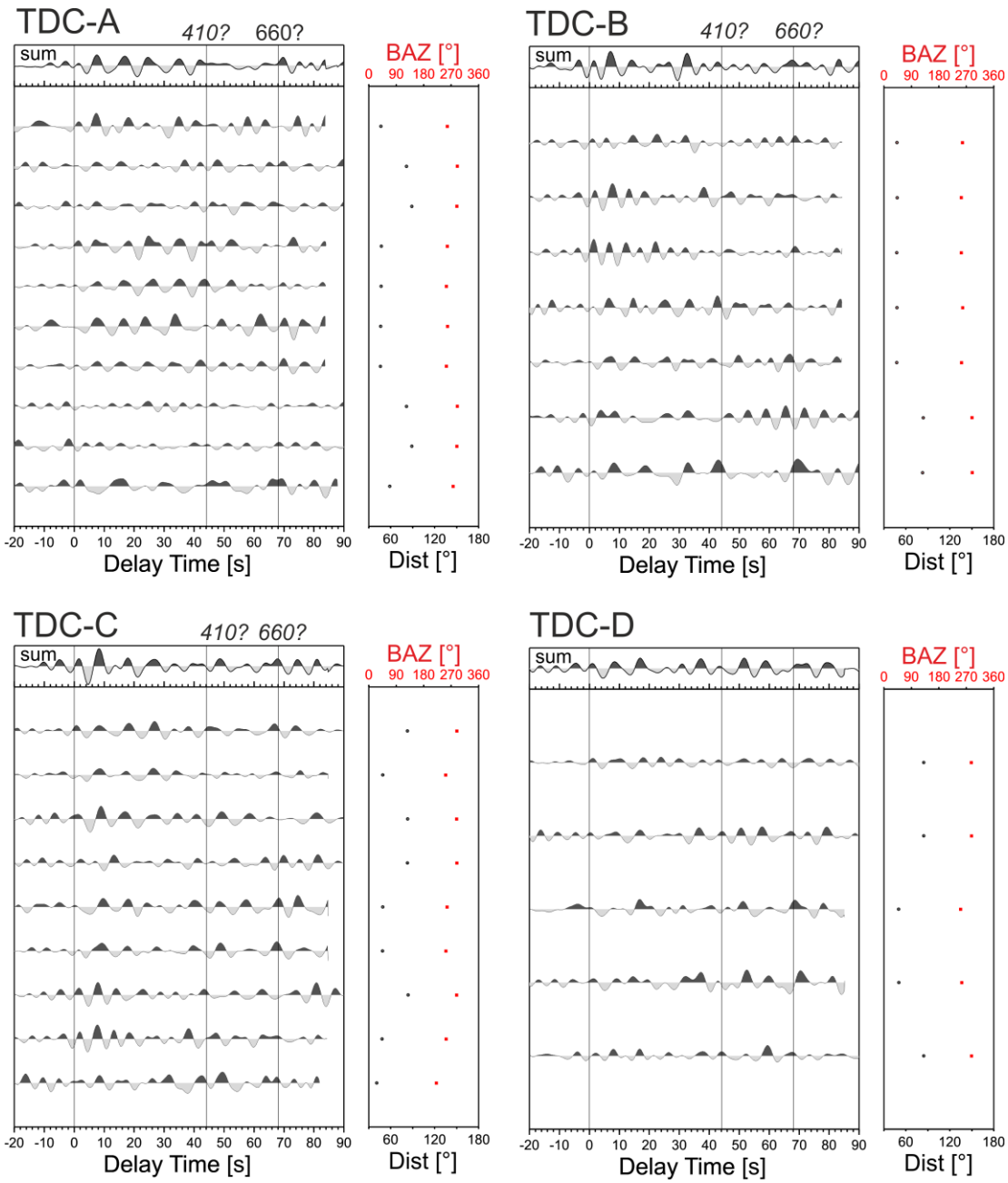

Appendix 6

a) model M3 (with water layer)

layer	depth [km]	Vp [km/s]	Vs [km/s]	ρ [g/cm3]	Qp	Qs
1	0	1.5	0.01	1	9999	1
2	3	1.5	0.01	1	9999	1
3	3	6.2	3.5	2.9	1340	600
4	10	6.2	3.5	2.9	1340	600
5	10	8.04	4.47	3.3	1340	600
6	35	8.04	4.47	3.3	1340	600
7	35	8.04	4.47	3.3	1340	600
8	71	8.044	4.483	3.375	1464.1	607.1
9	120	8.05	4.5	3.371	195	80
10	120	7.648	4.275	3.371	195	80
11	210	8.3	4.518	3.361	195.8	80.3
12	271	8.523	4.628	3.436	365.2	143
13	410	9.03	4.87	3.543	365.8	143
14	410	9.36	5.07	3.724	365.8	143
15	471	9.565	5.199	3.787	364.6	143
16	660	10.2	5.6	3.992	362.2	143.1
17	660	10.79	5.95	4.381	362.2	143.1
18	671	10.819	5.979	4.381	758	312
19	760	11.056	6.209	4.436	732.1	312
20	821	11.164	6.256	4.474	730.1	312
21	921	11.335	6.329	4.533	740.9	312
22	1021	11.498	6.397	4.592	746.3	312
23	1121	11.653	6.462	4.649	752.7	312
24	1221	11.801	6.524	4.706	757.9	312
25	1321	11.944	6.582	4.762	763.7	312
26	1421	12.08	6.637	4.817	767.9	312
27	1521	12.212	6.691	4.871	772.5	312
28	1621	12.34	6.742	4.924	777	312
29	1721	12.463	6.791	4.977	781.5	312
30	1821	12.584	6.838	5.029	786.1	312
31	1921	12.702	6.885	5.08	790.1	312
32	2021	12.819	6.931	5.13	793.5	312
33	2121	12.934	6.976	5.182	796.9	312
34	2221	13.048	7.021	5.232	801	312
35	2321	13.163	7.066	5.282	805	312
36	2421	13.278	7.112	5.332	809	312
37	2521	13.394	7.158	5.382	813	312
38	2621	13.513	7.206	5.432	816.9	312
39	2740	13.656	7.265	5.491	822	312
40	2771	13.664	7.272	5.506	823	312
41	2889	13.691	7.302	5.556	826	312
42	2889	8.009	0	9.903	57822	0
43	2971	8.15	0	10.029	57822	0
44	3171	8.477	0	10.327	57822	0
45	3371	8.777	0	10.602	57822	0
46	3571	9.05	0	10.853	57822	0
47	3771	9.295	0	11.083	57822	0
48	3971	9.514	0	11.293	57822	0
49	4171	9.706	0	11.483	57822	0
50	4371	9.871	0	11.655	57822	0
51	4571	10.009	0	11.809	57822	0
52	4771	10.12	0	11.947	57822	0
53	4971	10.204	0	12.069	57822	0
54	5153.9	10.258	0	12.166	57822	0

b) model M4 (without water layer)

layer	depth [km]	Vp [km/s]	Vs [km/s]	ρ [g/cm3]	Qp	Qs

3	0	6.2	3.5	2.9	1340	600
4	7	6.2	3.5	2.9	1340	600
5	7	8.04	4.47	3.3	1340	600
6	35	8.04	4.47	3.3	1340	600
7	35	8.04	4.47	3.3	1340	600

…

Appendix 7

a) tdc26_2.1b

depth [km]	vp [km/s]	vp/vs	n
0	4.5	1.8	1
2.5	5.3	1.8	5
2.5	6	1.8	0
5.5	6.3	1.8	5
5.5	8	1.8	5
40	8	1.8	10
200	8	1.8	10

b) nig01_2.1b

depth [km]	vp [km/s]	vp/vs	n
0	4.5	1.8	1
3	5.4	1.8	5
3	6	1.8	0
6	6.5	1.8	5
6	7.9	1.8	5
12	7.9	1.8	5
12	7.9	1.8	0
40	7.9	1.8	10
200	8	1.8	10

c) nig01_2.1c

depth [km]	vp [km/s]	vp/vs	n
0	4	1.8	1
2.5	4.5	1.8	5
2.5	5.5	1.8	0
5	6	1.8	5
5	6.5	1.8	0
18	6.9	1.8	5
18	7.9	1.8	0
40	7.9	1.8	10
200	8	1.8	10

c) nig01_2.1d

depth [km]	vp [km/s]	vp/vs	n
0	4	1.8	1
2.5	4.5	1.8	5
2.5	5.5	1.8	0
5	6	1.8	5
5	6.5	1.8	0
7	7.2	1.8	2
9	7.2	1.8	2
10	6.5	1.8	5
12	6.5	1.8	5
12.5	7.2	1.8	5
14	7.2	1.8	5
16.5	6.5	1.8	5
17.5	6.6	1.8	5
19	7.9	1.8	5
40	7.9	1.8	10
200	8	1.8	10

e) tris_2.1b

depth [km]	vp [km/s]	vp/vs	n
0	4.5	1.80	1
3	5.4	1.80	5
3	6	1.80	0
8.5	6.5	1.80	5
9.5	7.9	1.80	5
12	7.9	1.80	5
12	7.9	1.80	0
50	7.9	1.80	3
200	8	1.80	10

f) tris_2.2c

depth [km]	vp [km/s]	vp/vs	n
0	4.5	1.8	1
3	5.4	1.8	5
3	6	1.8	0
9	6.5	1.8	5
9	7.9	1.8	0
45.5	7.9	1.8	3
45.5	7.2	1.92	0
200	7.2	1.92	1

g) tris_2.3b

depth [km]	vp [km/s]	vp/vs	n
0	4.5	1.8	1
3	5.4	1.8	5
3	6	1.8	0
9	6.5	1.8	5
9	7.9	1.8	0
50	7.9	1.8	3
60	7.6	1.85	5
65	7.6	1.92	5
105	7.6	1.92	10
115	8.2	1.82	3
135	8.2	1.82	5
139	7.2	1.9	5
148	7.2	1.9	1
152	8.2	1.82	5
200	8.2	1.82	1

Appendix 8

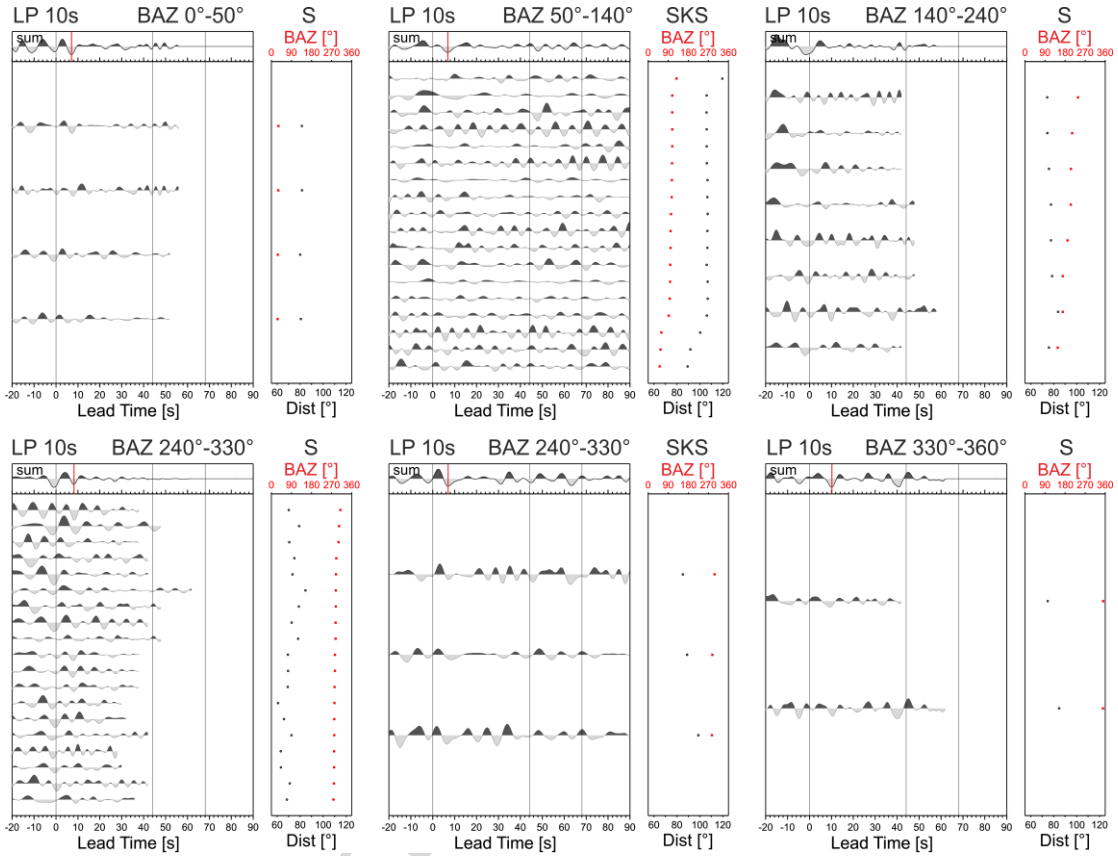

Table 1

Station	latitude (deg)	longitude (deg)	elevation (m)	orientation (deg)	t_{Ps} (s)	t_{pPs} (s) LP 1s	$t_{Ps+PpSs}$ (s)	n	$t_{Ps+PpSs}$ (s) LP 2s	n	$t_{Ps+PpSs}$ (s) LP 3s	n	$t_{Ps+PpSs}$ (s) LP 5s	n	Δt (s)	H (km) Vp=6.0 km/s	Vp/Vs	n	LP (s)
TDC01	-35.925	-9.686	-394	20		2.1	4.03	3	4.48	8	4.34	4	**4.15**	**5**	0.3				
TDC02	-36.699	-9.994	-363	-40		2.3	3.42	2	**3.85**	**5**	4.04	4	3.76	6	0.3				
TDC03	-37.592	-10.309	-358	-35		1.5	3.72	2	**3.72**	**2**	3.82	2	*5.17*	*7*	*0.1*	5.18	1.91	2	2
TDC04	-38.364	-10.782	-345	25		1.4	4.03	3	**4.32**	**2**	3.82	2	3.64	4	0.7	7.4	1.79	2	2
TDC05	-38.581	-11.962	-316	5?	1.1	2.1	3.42	2	**3.84**	**2**	3.84	2	3.43	3	0.5	5.5	1.85	2	2
TDC06	-37.747	-11.374	-356	180	0.9		3.84	4	**4.00**	**3**	3.76	6	3.46	6	0.6	6.4	1.93	4	2
TDC07	-36.908	-11.206	-379	170	0.9	2.9	4.51	1	**3.15**	**5**	3.46	6	-	7	0.3	4.9	1.92	5	2
TDC0	-3	-10.8	-3	noisy															

8	6.13	03	95																					
	32		1																					
	-3		-																					
	5.6		41																					
TDC09	43	11.495	69	no X																				
	-3		-																					
	6.2		37		1	2											0	5	1.					
TDC10	76	11.940	13	5	.0	.3	4.4	3	**3.8**	**4**	4.1	3	4.4	4	.6	.9	8	8	4	1				
	-3		-																					
	6.8		35		1	2											0	6	1.					
TDC11	78	12.122	70	200	.3	.8	3.9	3	**4.0**	**1 0**	4.1	8	4.1	1 0	.1	.4	8	1	0	2				
	-3		-																					
	7.3		36		1	3											0	*4*	*1.*					
TDC12	61	11.902	74	235	.9	.4	4.6	5	**4.9**	**6**	5.2	5	4.9	6	.3	*.7*	*8*	*4*	6	2				
	-3		-																					
	7.9		33				3.1	3	**3.2**	**6**	3.7	4	3.2	5	0. 5									
TDC14	30	12.452	08	150																				
	-3		-																					
	8.7		31	-											*0*									
TDC15	53	13.082	84	150					*3.8*	*2*			***3.3***		*.5*									
	-3		-																					
	8.9		30																					
TDC16	02	14.012	99	no X																				
	-3		-	no																				
	8.0		33	t																				
TDC17	83	13.639	80	re co v.																				
	-3		-																					
TDC18	7.59	12.913	16 0	no XY																				

TDC19	-37.257	-13.418	-358.80	80	0.4	2.1	3.73		***3.77***		*3.84*		*4.83*		16.*1*	16.10	1.84	7	2		
TDC20	-38.274	-14.722	-324.4	-45	0.4	1.5	3.36		**3.35**		3.77		4.27		05.09	05.4	1.83	6	2		
TDC21	-37.611	-15.621	-329.9	no data																	
TDC22	-37.481	-14.549	-342.2	140	0.7	1.9	3.34		4.08		4.610		**4.08**		05.6	05.4	1.84	8	2		
TDC23	-36.647	-14.284	-367.2	-10	12.1	2.1	3.71		***3.91***		*4.34*		*4.55*		*0*6.6	06.8	1.76	1	1		
TDC25	-36.403	-13.047	-355.2	not recov.																	
TDC26	-36.995	-12.679	-350.3	160	0.7	2.1	3.74		**3.85**		3.17		3.86		04.67	04.8	1.86	5	1		
TDCXX						2.11	3.61	50	**3.81**		3.79		4.12	10	05.23	05.8	1.87	8	12		
TDCXX-NE		(TDC01, 02, 07, 10)				2.13	3.99		**3.72**	**2**	4.15		4.12	2	05.24	05.7	1.89	2	2		
TDCXX-SE		(TDC03, 04, 05, 06)				2.2	3.61	11	**3.89**		3.62		4.00	20	06.4	06.3	1.88	9	2		

TDCX-SW		(TDC14, 15, 20)				1.5	3.2	10	**3.4**	**13**	3.7	12	3.7	15	0.3	5.5	1.82	13	2	
TDCX-NW		(TDC19, 22,23)				2.0	3.7	8	**3.7**	**16**	4.2	18	4.4	16	0.7	9.7	1.87	16	2	
NIG01	-37.418	-12.456	40	-23.5	0.6	2.0	4.8	2	**5.2**	**23**	4.3	34	4.0	6	1.2	8.7	1.81	3	2	
TRIS	-37.058	-12.316	0	-85	0.8	3.9	6.2	31	**6.1**	**30**	5.8	34	6.2	45	0.4	9.4	1.78	30	3	

Table 2

Station/Area	t_{P410s} (s)	t_{P610s} (s)	$t_{P610s-2}$ (s)	dt_{MTZ} (s)	dt_{MTZ-2} (s)	n
TRIS-NE	-	67.5		-		14
TRIS-S	45.3	65.6	72.1	20.3	26.8	16
TRIS-NW	**43.7**	**69.0**		**25.3**		**13**
TDC-A	*41.9*	69.7		*27.8*		10
TDC-B	*42.8*	67.6		*24.8*		7
TDC-C	*48.6*	*67.9*		*19.3*		9
TDC-D	-	-		-		5

Table 3

Phase	BAZ	LP 7s				LP10s			
		t_{SMp} (s)	t_{SLABp} (s)	$t_{SLABp-2}$ (s)	n	t_{SMp} (s)	t_{SLABp} (s)	$t_{SLABp-2}$ (s)	n
S/SKS	0-360	0.6	8.1		30	3.5	8.0		64
S	0-360	1.3	8.0		14	3.9	**8.2**		37
SKS	0-360	-	8.3		16	2.3	**6.6**		27
S/SKS	0-50	2.5	5.8		4	2.9	7.1		4
S	0-50	2.6	5.6	7.9	3	2.9	**7.1**		4
SKS	0-50	2.0	6.2		1	-	-		-
S/SKS	50-140	0.4	8.3		9	2.5	6.5		21
S	50-140	1.4	8.1		1	2.9	5.3		3
SKS	50-140	-	8.4		8	2.1	**6.8**		18
S/SKS	140-240	-	-		9	*5.0*	-		14
S	140-240	*5.1*	*8.0*		3	4.8	*8.9*		8
SKS	140-240	-	-		6	-	-		6
S/SKS	240-330	1.4	*8.2*		7	3.8	*8.1*		22
S	240-330	1.0	*8.1*		6	4.2	**8.1**		19
SKS	240-330	2.2	*8.9*		1	*2.6*	***7.1***		3
S/SKS	330-360	*4.6*	*10.3*		1	*3.9*	*10.1*		2
S	330-360	*4.6*	*10.3*		1	*3.9*	*10.1*		2
SKS	330-360	-	-		-	-	**-**		-

Highlights

- Receiver functions from ocean-bottom seismometer stations reveal no significant crustal thickening in the surrounding of the Tristan da Cunha hot spot.
- The mantle transition zone to the NW of Tristan da Cunha is thickened and cool.
- The mantle transition zone is potentially thinned to the south/southwest of Tristan da Cunha.
- A thickness of 60 to 75 km beneath Tristan da Cunha argues for a compositional control on the seismological lithosphere in the South Atlantic.